Journal of Asian Earth Sciences: X 7 (2022) 100091

Contents lists available at ScienceDirect

Journal of Asian Earth Sciences: X

journal homepage: www.sciencedirect.com/journal/journal-of-asian-earth-sciences-x

# Quaternary dating and instrumental development: An overview

Upasana S. Banerji [a], Vineet Goswami [b,*], Kumar Batuk Joshi [a]

[a] National Centre for Earth Science Studies, Thiruvananthpuram-695 011, Kerala, India
[b] Physical Research Laboratory, Ahmedabad-380 009, Gujarat, India

ARTICLE INFO

*Keywords:*
Quaternary Period
Cosmogenic isotopes
Radiocarbon Dating
AMS
Exposure Age Dating
Lead-210

ABSTRACT

Reliable estimation of ages and temporal correlations through the Quaternary Period (<2.58 Myr) have led to a better understanding of paleoclimatic changes. Various dating techniques applicable through the Quaternary have received significant impetus from paleoclimate community for high-resolution climatic reconstructions that are supported by robust chronological controls. Radiometric dating of Quaternary samples/archives have extensively progressed due to significant instrumentation developments. The Quaternary studies involve several radiometric dating techniques which include cosmogenic and anthropogenically produced radioisotopes.

Radiocarbon ($^{14}C$) is a cosmogenically produced radionuclide that has been frequently used to date recent archives. Previously, conventional β counting method for radiocarbon dating required ~ 1 g of carbon extracted from the samples. However, with the introduction and development of Accelerator Mass spectrometry (AMS), it became possible to date these natural archives with a much smaller sample quantity. In addition to its application in $^{14}C$ dating, AMS also led to a breakthrough in application of other cosmogenic isotopic systems ($^{10}Be$, $^{26}Al$) to understand various earth surface processes (e.g., glacial retreats, denudation rates). The $^{210}Pb$ dating technique is mainly used to study anthropogenic forcing on annual to decadal climatic changes. The measurement technique for $^{210}Pb$ commenced with α detectors and involved tedious chemical separation and longer measurement times in attaining secular equilibrium. However, the gradual adoption of β and γ detectors led to rapid analysis with relatively shorter analysis times. This contribution aims to provide an overview of frequently used radiometric ($^{14}C$, $^{10}Be$, $^{26}Al$, $^{210}Pb$ and $^{137}Cs$) dating techniques in Quaternary studies and discusses the significant instrumental developments.

## 1. Introduction

The Quaternary Period is the most recent and shortest geological period that started around 2.58 Myr ago and is characterized by significant climate instabilities. The deep-sea sediment records have demonstrated around 50 glacial and interglacial stages over the regular 23, 41, and 100 kyr cyclicities through the Quaternary, underscoring significant periodic climatic shifts with possible feedback mechanisms (Williams et al., 1998). However, the precise number of glacial-interglacial cycles is yet to be established from terrestrial records (Shackleton et al., 1990). The oxygen isotope study based on foraminifera from the marine sediment cores has revealed a consistently changing ocean–atmosphere system during the past. The climatic instability as a function of oxygen isotopic variations for each oscillation was first reported by Emiliani (1955). The marine isotopic records indicate that until 0.9 Myr, the expansion and contraction of the Greenland and Antarctica ice sheet primarily followed a 41 kyr cyclicity, coinciding with the earth's obliquity. Further, the glacial periods during the late Quaternary showed a periodicity of around 100 kyr (Fig. 1), displaying slow and uneven cooling followed by a rapid deglaciation. Additionally, along with the overall long-term cooling, which lasted for around 70–90 kyr, there were several high-frequency warmer episodes (interstadials) with unusually cold periods in between (called stadials; Williams et al., 1998). The irregular climatic cyclicity that occurred during the late Quaternary Period calls for a need to understand the processes, mechanisms, and feedbacks responsible for such climate perturbations (Fig. 1). One of the basis for precisely understanding these climatic variabilities and their underlying mechanisms involves reliable chronological controls and precise temporal correlations by appropriate radiometric dating techniques.

In general, various radiometric dating methods (e.g., Rb-Sr, Sm-Nd, Re-Os, U-Pb, K-Ar) have been used to estimate the ages of various rocks and minerals spanning significant portions of the geological timescale (Crawford, 1970; Goswami et al., 2018; Hannah et al., 2004; Joshi et al.,

* Corresponding author.
*E-mail address:* vineetg@prl.res.in (V. Goswami).

https://doi.org/10.1016/j.jaesx.2022.100091
Received 12 April 2021; Received in revised form 8 February 2022; Accepted 17 March 2022
Available online 21 March 2022
2590-0560/© 2022 Published by Elsevier Ltd. This is an open access article under the CC BY-NC-ND license (http://creativecommons.org/licenses/by-nc-nd/4.0/).

2017, 2021a; Samom et al., 2018; Tripathy et al., 2018). Further, considering the Quarternary Period, the chronological methods can be broadly categorized into three groups: qualitative and comparative, radiative dosimetry, and radiometric (Hajdas et al., 2008; Jull, 2014). The qualitative and comparative methods rely on the relative incremental growth in the natural archive with time. A few examples of qualitative and comparative dating methods include dendrochronology, sclerochronology, varve sediments, and isotopic composition ($\delta^{18}O$) correlations in ice cores and sedimentary cores. Additionally, the build-up of radiation damage within some minerals (quartz, feldspar) in natural archives can be used to determine the time elapsed since the last exposure to sunlight or sufficient heating, forming the basis of the

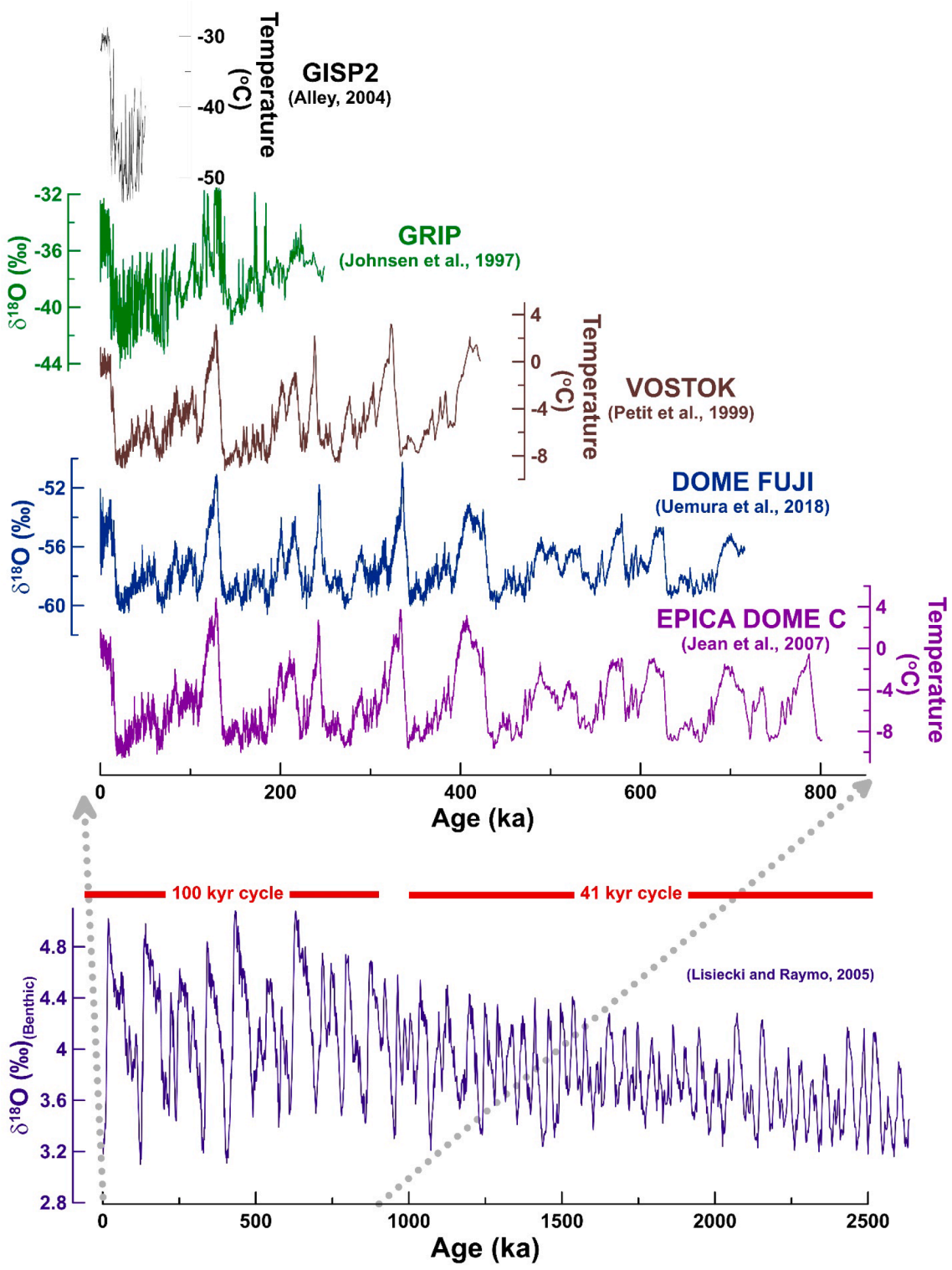


**Fig. 1.** Stacked $\delta^{18}O$ of foraminifera showing a cyclicity of 41 kyr during 2500–1000 ka and 100 kyr during last 900 ka (Lisiecki and Raymo, 2005). Compilation of Antarctica (DOME FUJI, VOSTOK, and EPICA DOME C) (Jouzel et al., 2007; Petit et al., 1999; Uemura et al., 2018) and Greenland (GISP2 and GRIP) (Alley, 2004; Johnsen et al., 1997) ice core data for temperature and Oxygen isotopes ($\delta^{18}O$).

luminescence dating techniques: thermoluminescence (TL) and Optically Stimulated Luminescence (OSL). The last decade has witnessed several developments in the luminescence dating techniques, e.g., the development of thermally transferred OSL (TT-OSL) and violet stimulated luminescence (VSL) for quartz (Jain, 2009; Wang et al., 2006). Further, in order to extend the dating range up to early Pleistocene post-infrared infrared stimulated luminescence (pIRIR) at elevated temperatures up to 290 °C was introduced for alkali feldspars (Thomsen et al., 2008). In the present contribution, we have mainly focussed on dating techniques based on radiometric measurements, and thus the luminescence techniques have not been discussed any further.

Several radiometric dating techniques have been applied to date the formation/deposition timing of various natural archives (e.g., foraminiferal tests, sediments, corals, speleothem, ice cores) spanning the Quaternary Period. The spontaneous decay of radioactive parent isotope into the radiogenic daughter and the emission of particles is termed radioactive decay (Banner, 2004). Most radioactive isotopes produced in nucleosynthesis during stellar evolution decayed during the geologic past and became extinct. However, the existance of radioactive isotopes in the geological materials could be due to one of the following cases: (i) radioisotopes having half-life longer than the earth's age; (ii) the radioisotope is the daughter product of the radioactive parent having a long half-life; (iii) radioisotopes produced by interaction with the cosmic rays, and (iv) anthropogenically produced artificial radioisotopes (Banner, 2004).

The sediments that accumulate over time into various water bodies (e.g., in the ocean, lakes, estuaries, wetlands) act as imperative archives of past climatic changes. Depending on their depositional environments, the sediment deposition rates can vary widely, from a few millimeters to centimeters per year. In contrast to other paleoclimatic archives (e.g., speleothems, corals, ice cores) that grow in specific zones, the ubiquitous nature of sediments makes them the frequently used archives to investigate the past climatic changes. Further, to link various sedimentary chemical and isotopic signatures with past climatic events, it becomes essential to understand the deposition rates of sediments and their temporal correlations. In this context, several dating techniques can be used to address the chronology of sediment deposition. These dating techniques rely on natural, artificial, or cosmogenic radionuclides. Once precise chronological constraints on the sediments have been established, these sedimentary archives can be efficiently used to reconstruct and understand the variations in climatic patterns and their global linkages (Banerji et al., 2019). In the present contribution, we discuss in detail some of these radiometric dating methods applicable through the Quaternary Period to constrain the depositional/formation ages of natural systems and estimate the exposure ages and denudation rates. The radiometric dating methods include cosmogenic radionuclides such as radiocarbon ($^{14}$C), beryllium-10 ($^{10}$Be) and aluminium-26 ($^{26}$Al) and short-lived radionuclides such as lead-210 ($^{210}$Pb) and caesium-137 ($^{137}$Cs). The $^{137}$Cs radionuclide is produced as one of the common fission products by the nuclear fission of $^{235}$U. The frequent human intervention in natural systems by nuclear tests provided significant thrust in developing the $^{137}$Cs (half-life ~ 30.17 years) dating technique that can constrain the sediment chronology for the last few decades. The abundant presence of carbon in sediments in the form of organic and inorganic fractions exalted the implications of the radiocarbon ($^{14}$C) method. At the same time, the need to address the timing of various earth surface processes, e.g., glacial retreats (exposure ages) and erosion/denudation rates promoted the applicability of the $^{10}$Be and $^{26}$Al in earth science studies. These radiometric methods have served as a key to unlocking the climatic episodes during the late Quaternary Period. In the field of radiometric geochronology, the analytical accuracy and precision simultaneously progressed with significant developments in nuclear science and instrumentation. Thus, in the present contribution, we have also provided an overview of instrumental techniques (radiation spectroscopy, AMS) used in the radiometric dating techniques relevant to the Quaternary Period.

## 2. Natural and artificial radionuclides

### 2.1. Lead-210 ($^{210}$Pb)

In the early 1970s, the breakthrough in paleolimnology and dating of recent sediments deposited during the last century became possible with the discovery of the $^{210}$Pb dating technique and estimation of artificial fallout radionuclides (Appleby, 2008). The $^{210}$Pb dating method was initially proposed by Goldberg, (1962). Subsequently, the $^{210}$Pb technique was applied to understand (i) the accumulation history of Antarctic snow (Crozaz et al., 1964), and (ii) sediment deposition and accumulation records in deep-sea environments (Koide et al., 1973, 1972). Simultaneously, the applicability of $^{210}$Pb dating was extended to understand the depositional history of lake sediments (Krishnaswamy et al., 1971). The $^{210}$Pb concentration in the atmosphere is regulated by its various sources, atmospheric circulation pathways, and deposition mechanisms (Fig. 2) (Preiss et al., 1996).

The $^{210}$Pb dating has been an efficient geochronological tool for paleoenvironmental reconstructions spanning the last two centuries. Using the $^{210}$Pb dating technique and assuming that the surface/top sedimentary layers are deposited during the year of sample collection, sedimentation rates of rapidly depositing sedimentary layers can be estimated. $^{210}$Pb is a naturally occurring radionuclide that forms as a decay product within the $^{238}$U decay series. $^{210}$Pb eventually decays with a short half-life of 22.3 years. The $^{238}$U present in the earth's crust decays to $^{226}$Ra through a series of intermediate radionuclides, which is followed by subsequent decay to $^{222}$Rn, a gaseous radionuclide that escapes to the atmosphere. Subsequently, $^{222}$Rn (half-life = 3.8 days) further decays to $^{210}$Pb through several intermediate radionuclides with short half-lives ranging from 0.16 s to 20 min (Fig. 2). Once formed in the atmosphere following this decay chain, $^{210}$Pb returns to the earth's surface primarily by wet deposition and is introduced to the ice, marine, and lacustrine systems. The inter-hemispheric $^{210}$Pb fallout rates over the oceanic regions vary significantly from 0.003 to 0.35 mBq m$^{-3}$ in the northern hemisphere while lying between 0.012 and 0.12 mBq m$^{-3}$ in the southern hemisphere (Preiss et al., 1996).This *excess* $^{210}$Pb supplied to the system from the external source(s) is deemed unsupported $^{210}$Pb. In contrast, the $^{210}$Pb fraction forming *in situ* in the sediments as a decay product of sedimentary $^{238}$U is termed as supported $^{210}$Pb (Fig. 2). To estimate the unsupported/excess $^{210}$Pb (noted as $^{210}Pb_{xs}$) in the system, $^{226}$Ra activity is deducted from the total $^{210}$Pb activity, assuming that both supported $^{210}$Pb and $^{226}$Ra in sediments are in secular equilibrium (Appleby and Oldfield, 1992; Pheiffer Madsen and Sørensen, 1979). Decay from $^{222}$Rn is the primary source of $^{210}$Pb. Upon decay from $^{226}$Ra (half-life = 1602 years), $^{222}$Rn escapes from the earth's surface with a mean emission rate of around one atom cm$^{-2}$ s$^{-1}$ from ice-free continental regions. However, $^{222}$Rn does not easily escape through the ice; thus, ice-covered regions are not considered as significant sources of $^{210}$Pb. This model has been widely accepted in several cases, especially in stable environments such as the region with constant sediment accumulation rates. Nevertheless, this emission model has also been accepted in regions with inconsistent accumulation rates. However, an appropriate dating model is required to ascertain the sedimentation rate (Appleby, 1997).

Based on the radioactive decay equation ($N = N_0\ e^{-\lambda t}$; wherein N represents remaining radioactive nuclides after time 't', and $N_0$ represents initial radioactive nuclides), there are three models proposed for the $^{210}$Pb chronology: (i) the Constant Flux:Constant Sedimentation (CF:CS) (Krishnaswami et al., 1971), (ii) Constant Rate of Supply (CRS) (Appleby and Oldfield, 1978), and (iii) Constant Initial Concentration (CIC) (Robbins, 1978). These models are based on similar assumptions: (a) the $^{210}Pb_{xs}$ deposition is at a steady state, (b) no post-depositional mobility of $^{210}$Pb from the system, and (c) new $^{210P}b_{xs}$ input supply above the previously deposited layer(s).

The CF:CS model assumes a constant deposition flux of $^{210}Pb_{xs,}$ and mass accumulation rate (MAR) such that the $^{210}$Pb specific activity at the

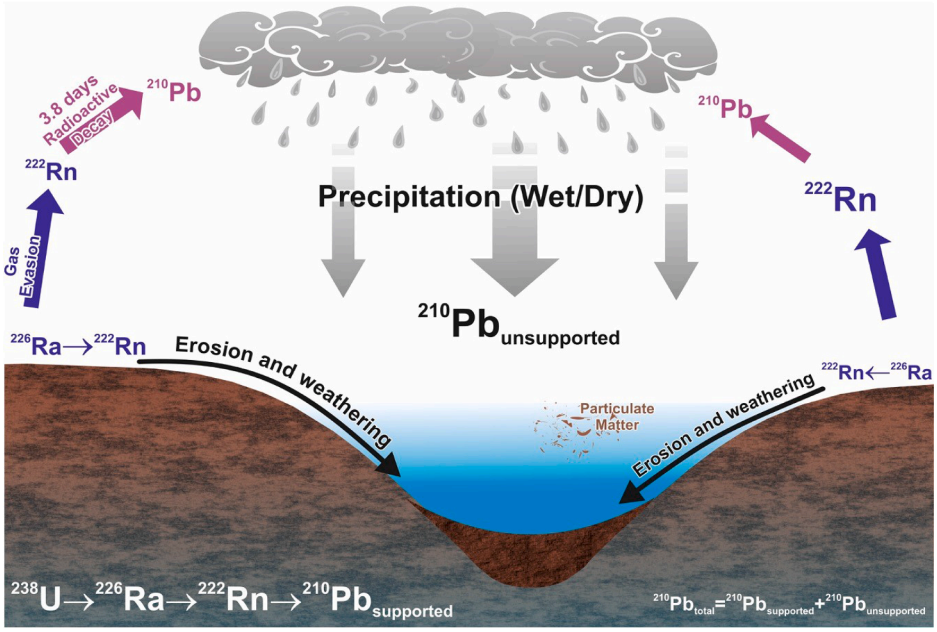


**Fig. 2.** Schematic of $^{210}$Pb dating wherein the unsupported $^{210}$Pb results from the escape of $^{222}$Rn gas into the atmosphere and later brought back to the earth's surface via precipitation (wet/dry). While the supported $^{210}$Pb forms due to the decay of $^{226}$Ra to $^{210}$Pb via $^{222}$Rn gas.

surficial sediments is consistent, decreasing exponentially with depth in the sedimentary column (Arias-Ortiz et al., 2018; Goldberg et al., 1977). However, $^{210}$Pb accumulation rates could be variable due to several natural and/or anthropogenic factors. Under sedimentray conditions with such variable accumulation rates, CRS or CIC is more applicable. In the CRS model, a constant flux of $^{210}$Pb is assumed throughout the deposition time. In CRS, the initial specific activity is inversely proportional to the MAR. Thus, the dating relies on comparing $^{210}$Pb$_{xs}$ inventories below specific depths with the overall inventory of $^{210}$Pb$_{xs}$ in a sediment core. However, the applicability of the CRS model requires an accurate estimation of the $^{210}$Pb$_{xs}$ inventories (Appleby, 2001).

The CIC model, in particular, is found to be more appropriate for the locations where the deposited sedimentary layers are influenced by significant hydrological changes or any hiatus caused by erosion events (Appleby, 2008). The CIC model assumes constant time-invariant initial $^{210}$Pb$_{xs}$ specific activity at the sediment–water interface independent of sedimentation rate. Thus, $^{210}$Pb$_{xs}$ flux simultaneously varies with the MAR. CIC allows estimating the age of the sampled sedimentary layers where the $^{210}$Pb activity has been measured, provided the initial specific activity is known. The CIC model considers a continuous decline in the $^{210}$Pb$_{xs}$ specific activity to avoid age reversals. Thus, the model may not efficiently apply to sediments depositing in coastal regions. Generally, the CRS model is more applicable in estuarine, coastal, and lacustrine environments, while CIC and CF:CS have been typically applied to purely marine environments (Andersen, 2017; Arias-Ortiz et al., 2018; Breithaupt et al., 2014).

Due to the inverse relationship between the sediment grain size and grain surface area, muddy sedimentary environments are typically characterized by the highest adsorbed $^{210}$Pb activities (Smith and Walton, 1980). Thus, a prior understanding of the instrumental analytical detection limits and sample size, along with the grain size, is required before subsampling a sediment core for the $^{210}$Pb analyses to estimate sedimentation rates (Kirchner, 2011). A thinner subsampled sedimentary section can provide better time resolution at the expense of limited $^{210}$Pb counting statistics. Usually, in a sedimentary column, the accumulated $^{210}$Pb$_{xs}$ activity is a function of $^{210}$Pb$_{xs}$ flux into the sediment and is linked inversely to the sedimentation rate (Alexander and Lee, 2009). A tentative sedimentation rate for a sediment core can provide significant insights into sectioning of the sediment core. Otherwise, the sediment core can be sectioned into thin layers (starting from younger/top to older/deeper section) and tested for $^{210}$Pb$_{xs}$ activities. When the $^{210}$Pb$_{xs}$ activities begin to display values close to the instrumental detection limits, multiple sediment sections can be combined and measured for $^{210}$Pb$_{xs}$ (Kirchner, 2011).

The $^{210}$Pb$_{xs}$ distribution in the sedimentary column is influenced by several factors: post-depositional $^{210}$Pb diffusion, bioturbation, sediment compaction, sediment grain size, sediment remobilization, and material/sediment loss during sampling. Further, various anthropogenic activities such as wastewater discharge, ship traffic, near-shore recreational activities can provide an additional source of $^{210}$Pb (Kirchner, 2011).

Over the Indian subcontinent, the $^{210}$Pb concentration in surface air decreases from north to south (1 to 0.5 mBq m$^{-3}$). High and homogenous $^{210}$Pb concentrations have been observed in the northern India, while a southward decrease has been attributed to the increased marine influence surrounding the Indian peninsula (Preiss et al., 1996). Likewise, the $^{210}$Pb air-surface deposition flux over the Indian subcontinent shows a decreasing flux gradient from the north to south (182 mBq m$^{-2}$y$^{-1}$ to 85 mBq m$^{-2}$y$^{-1}$; Joshi et al., 1969). On a global scale, it has been observed that there is a consistent increase in $^{210}$Pb fallout from west to east within the major continents (Appleby, 1997).

### 2.2. Caesium-137 ($^{137}$Cs)

The large-scale surficial nuclear and thermonuclear tests conducted primarily in the Northern Hemisphere between 1951 and 1963 can be broadly divided into two phases: pre-and post-moratorium weapons testing years. The USA conducted large-scale nuclear tests during the pre-moratorium years (1952–1958), while during 1958–1961, the testing moratorium between the USA and the former Soviet Union temporarily ended. The peak in the global radionuclide fallout deposition was observed around 1963, accompanied by the resumption of nuclear testing (Fig. 3). Simultaneously, in 1963, the atmospheric nuclear testing programs was terminated by signing of the Limited Test Ban Treaty initially by the governments of the Soviet Union, the United Kingdom, and the United States (Buesseler, 1997). These nuclear tests led to the production of several artificial short-lived radionuclides ($^{137}$Cs, $^{90}$Sr, $^{241}$Am, $^{239}$Pu, $^{240}$Pu), which were initially dispersed in the

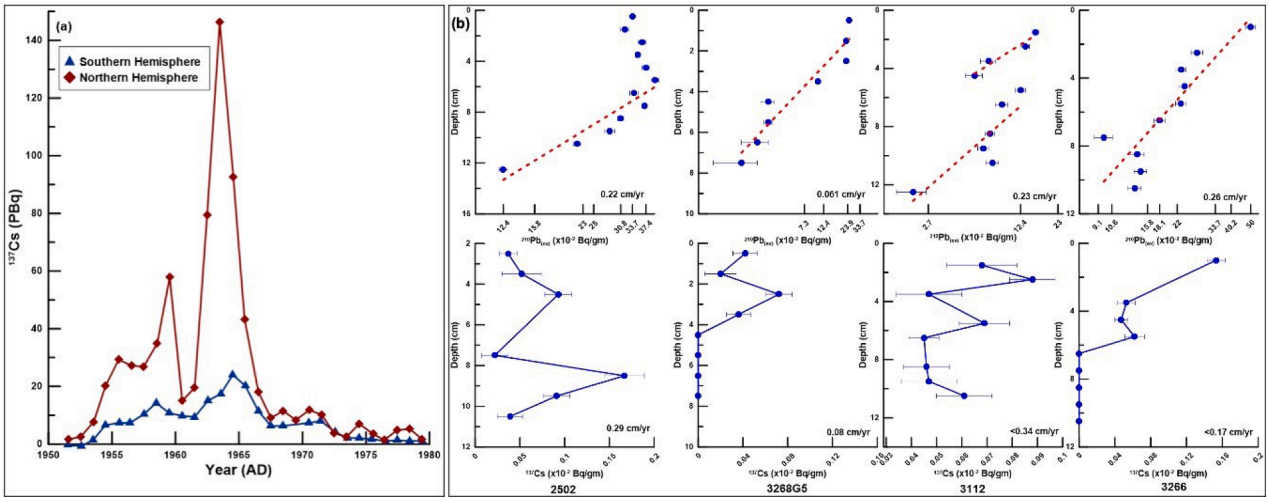


**Fig. 3.** (a) Historical fallout of $^{137}$Cs for the Northern and Southern hemispheres (UNSCEAR, 2000), wherein the peak is observed at ~ 1963 CE. (b) Sedimentation rates and age estimated for the sediment core retrieved from the western Indian continental shelf (Somayajulu et al., 1994).

atmosphere. Once released into the atmosphere, the airborne radionuclides can be advected away from their source regions to distal sites through their long-range atmospheric transport, subsequently leading to their fallout. Due to their atmospheric fallout, the short-lived artificial radionuclides later got incorporated into various earth surface systems (e.g., soil, water). These bomb-fallout short-lived radionuclides have been efficiently applied to date recent sediments and study environmental radioactivity (Abril Hernández, 2016).

Nuclear weapon testing has been considered as the primary source of atmospheric plutonium (Pu) and its fallout to the earth's surface (Kudo, 2001). The dominant long-lived Pu isotopes introduced into the atmosphere due to the nuclear tests were $^{239}$Pu and $^{240}$Pu, commonly represented as $^{239,240}$Pu (Buesseler, 1997). Data collection based on aerosol, soil, and ice cores suggests that the global average Pu fallout ratio ($^{240}$Pu/$^{239}$Pu) of 0.18 (Krey et al., 1976). However, significant variability in the $^{240}$Pu/$^{239}$Pu ratios has been reported from different test sites: e.g., the Nevada test site suggested a significantly lower ratio of 0.035 (Hicks and Barr, 1984), while Pacific Proving Grounds reported relatively higher ratios varying from 0.21 to 0.36 (Buesseler, 1997). During the 1950s, production and subsequent fallout of $^{90}$Sr was regarded as a significant cause of concern. The short-lived radionuclide of Sr, $^{90}$Sr (half-life ~ 29 years) is regarded as one of the most dangerous radionuclides due to its biological fixation in bones, leading to bone cancer (Garcia, 1980). Thus, the global deposition of $^{90}$Sr was widely monitored by the USA and UK during the 1950s and 1960s. In 1967, the obtained data were used to generate elaborate maps representing cumulative global $^{90}$Sr deposition (United Nations, 1969). Later, using the $^{90}$Sr fallout data, the fallout and deposition patterns for $^{137}$Cs were generated as the global fallout fluxes for the latter radionuclide were not widely documented (Garcia, 1980). Using these data, the nuclear test associated characteristic activity ratio of $^{90}$Sr/$^{137}$Cs was estimated to be around 0.60 (United Nations, 1982).

$^{137}$Cs is an artificial radionuclide produced during nuclear fission and has a half-life of ~30 years. The thermonuclear weapon tests starting in 1952 resulted in a significant injection of $^{137}$Cs into the stratosphere, leading to its widespread global dispersal (Perkins and Thomas, 1980). Once in the atmosphere, $^{137}$Cs was circulated and distributed globally via atmospheric circulation pathways (Longmore, 1982). Depending on the latitude, globally, the bomb-derived $^{137}$Cs fallout ranged between 160 and 3990 Bq m$^{-2}$ (Garcia Agudo, 1998). The $^{137}$Cs fallout is strongly related to local precipitation rates and patterns (Longmore, 1982). Extensively high $^{137}$Cs concentrations were observed in the atmosphere during 1963–1964 (Robbins and Edgington, 1975). Given this fact, the observed $^{137}$Cs activity maxima at a particular depth in the sedimentary column correspond to 1963 or 1964, precisely aligning with the time of maximum atmospheric fallout (Fig. 3a). In addition to this, sporadic and isolated incidents of accidental $^{137}$Cs release and dispersion into the atmosphere have been linked with noteworthy incidents of nuclear power plant disasters. Along with the more prominent nuclear test peak, these events can be observed as separate smaller $^{137}$Cs peaks in the sediments (Butler, 2011; Chino et al., 2011). Notable incidents such as Chernobyl and Fukushima Daiichi nuclear power plant disasters have highlighted the leakage of artificial radioactive nuclides such as $^{137}$Cs (Anspaugh et al., 1988; Koizumi et al., 2012).

The Chernobyl nuclear reactor accident happened on 26 April 1986, and the initial detection of radioactivity in the atmosphere was observed the following week in Sweden and Japan (Aoyama et al., 1986). The $^{137}$Cs fallout originating from Chernobyl affected various locations in the Europe and led to increased $^{137}$Cs inventory by several orders of magnitude at various global locations (Mabit et al., 2008). It has been estimated that nearly 13 EBq (1Ebq = $10^{18}$ Bq) of radioactive material was released during the accident (Baloga and Kholoscha, 2006; UNSCEAR, 1988), with a significant dose of $^{131}$I and $^{137}$Cs received by the population residing in the affected areas (Baloga and Kholoscha, 2006). The $^{137}$Cs isotope was used to understand the radiation leakage and contamination patterns, indicating that the territories of Belarus, Russia, and Ukraine were severely affected by accident and ensuing radiation leakage. An estimated total $^{137}$Cs activity of 64 TBq (1.7 MCi) was deposited in Europe, with Belarus, Russia, and Ukraine receiving around 23%, 30%, and 18% of radioactive contamination, respectively (Izrael et al., 1994). In addition, parts of Austria, Finland, Germany, Norway, Romania, and Sweden were also affected by the radioactive contamination (Saenko et al., 2011). The nuclear tests conducted during the 1950s mainly released $^{137}$Cs, whereas the Chernobyl event also led to the release of $^{134}$Cs. The characteristic $^{137}$Cs/$^{134}$Cs activity ratio of ~ 1:2 for Chernobyl-released Cs helped in discriminating it from nuclear test produced Cs (Livingston and Povinec, 2000).

The $^{137}$Cs peak in the sediments by the Chernobyl accident served as an excellent indicator for the short-term sediment accretion rates due to its high activity. The vertical accretion rates were primarily identified using $^{137}$Cs peaks of 1964 (nuclear tests) and 1986 (Chernobyl accident) for nearly five sediment cores raised from coastal wetlands of the North Sea and Baltic Sea (Callaway et al., 1996). A sediment core retrieved from the anoxic coastal regions of southern Rhode Island was chronologically constrained by $^{210}$Pb dating, sediment varve counting, and identifying the $^{137}$Cs peaks. The study showed twin $^{137}$Cs peaks coinciding with nuclear tests (1964) and the Chernobyl accident (1986). This

study documented the first known sedimentary record from North America that showed the Chernobyl-associated $^{137}$Cs peak (Lima et al., 2005).

The Fukushima Daiichi accident was another major nuclear power plant disaster that happened on 11 March 2011 due to the ensuing tsunami following the Tohoku earthquake. The accident resulted in enormous atmospheric radionuclide emissions (Butler, 2011; Chino et al., 2011). The released radioactive materials were subsequently transported to the ocean due to immediate oceanic discharge from the accident site or through atmospheric deposition (Tsumune et al., 2013). Based on a regional-scale simulation of $^{137}$Cs activity done for a year following the accident, the total amount of directly released $^{137}$Cs to the nearby ocean was estimated to be nearly 3.6 ± 0.7 PBq (Tsumune et al., 2013). During the accident, $^{137}$Cs dispersal was accompanied by $^{131}$I emissions. Model-based budget analysis showed that nearly 22% and 13% of $^{137}$Cs and $^{131}$I were respectively deposited over Japan, with the remaining proportions getting deposited over the ocean (Morino et al., 2011). Few models have estimated an amount ranging from 2.3 to 14.8 PBq of the radioactive Cs directly dispersed into the ocean (Kawamura et al., 2011; Rypina et al., 2013; Tsumune et al., 2012). However, the large variation in the estimated $^{137}$Cs amount is primarily due to the lack of observations in the oceanic region (Kaeriyama et al., 2014). The total $^{137}$Cs inventory accumulated in the top 3 cm of the surface sediments off the coasts of Miyagi, Fukushima, and Ibaraki prefectures indicated around 0.04 PBq of total $^{137}$Cs flux from the nuclear plant to the ocean following the accident (Kusakabe et al., 2013).

The anthropogenically induced $^{137}$Cs in conjunction with $^{210}$Pb has been a vital tool in estimating the chronology of the sedimentary section. Recently, the interlaboratory comparison of $^{210}$Pb dating suggested that the simultaneous use of $^{137}$Cs with the $^{210}$Pb age model resulted in reliable ages at least for the last 60 years (Barsanti et al., 2020). The study using both $^{210}$Pb and $^{137}$Cs on the lake sediment core (~40 cm) from Bosten Lake, China, revealed significant water level fluctuations during the last century due to changing climatic and anthropogenic influences (Ma et al., 2020). Further, a study based on $^{210}$Pb and $^{137}$Cs dating of sediment cores from Lagoa dos Patos, southern Brazil, demonstrated a strong influence of the Guaíba River discharge on the sediment transport into the lagoon interiors, resulting in variable sedimentation rates in northern and southern ends (Ivanoff et al., 2020). Another study from eight different lakes in the middle and lower reaches of the Yangtze river revealed an increase in the sedimentation rates after the 1950s, suggesting the simultaneous applicability of $^{210}$Pb and $^{137}$Cs in estimating the sedimentation rates (Xiang et al., 2002). However, this study raised apprehensions on applying these techniques during the seasonal hydrological water exchange between the Yangtze River and lakes. Further, the recent accumulation rates during the last century on a spatial scale were accessed based on several gravity cores raised from Ba Lat pro-delta, Red River, Vietnam (van den Bergh et al., 2007). This study underscored the effect of grain size fluctuations on the $^{210}$Pb activities, demonstrating high accumulation rates at the frontal pro-delta region and proximal part of the southern pro-delta region. Based on $^{210}$Pb dating of several sediment cores collected from the Arabian Sea (off Gujarat and Maharashtra), the sedimentation rates were estimated to be varying from 0.33 to 1.41 mm yr$^{-1}$ (Somayajulu et al., 1994). Further, using the $^{210}$Pb, $^{137}$Cs, and $^{14}$C dating techniques, the sediment deposition rates along the continental margins of the Arabian Sea were estimated to be around 0.5–6.6 mm yr$^{-1}$ for core depths of ≤ 10 cm, decreasing to 0.04–1.3 mm yr$^{-1}$ for depths > 10 cm (Fig. 3b), (Somayajulu et al., 1999). A study on mudflats from the central west coast of India showed low sedimentation rates of 0.13–2 cm yr$^{-1}$ till 1980, followed by an increased sedimentation rate of 1.2–2 cm y$^{-1}$ towards the top (Singh et al., 2014). A recent study along the western Indian continental shelf suggested that most sedimentation in the continental shelf of western India is due to the sediments brought by the rivers during the Indian summer monsoon (Shah et al., 2020). Additionally, higher sedimentation rates were observed along the southern continental shelf (off Kochi) in contrast to the northern continental shelf (off Goa) due to a combination of high riverine flux and longshore sediment transport (Shah et al., 2020). Despite its wide usage in chronologically constraining the sedimentary section deposited in last few decades, several factors such as the changing grain size, seasonal hydrological water exchange and high sediment accumulation rates can lead to problems with estimation of accurate sediment depositional ages, possibly resulting in misleading interpretations.

## 3. Cosmogenic radionuclides

The earth's atmosphere and surface are exposed to a flux of cosmic rays, which includes protons and α-particles from the Sun and other galactic sources (Watchman and Twidale, 2002). These cosmic rays induce a cascade of nuclear interactions in the atmosphere, eventually producing atmospheric cosmogenic radionuclides such as $^{14}$C, meteoric $^{10}$Be. Further, neutron-induced spallation reactions lead to the production of $^{26}$Al and $^{36}$Cl in the air (Watchman and Twidale, 2002). The cosmogenic radionuclides are of the lighter elements with varying half-lives. Most cosmogenic radionuclides remain attached to the aerosol particles, subsequently depositing on the earth's surface, except few gaseous species ($^{14}$C and $^{39}$Ar), which remain in the atmosphere (Lehto and Hou, 2011). The following sections discuss the basic concepts and applications of radiocarbon ($^{14}$C) and *in-situ* cosmogenic radionuclides ($^{10}$Be, $^{26}$Al) in constraining the timing of various earth system processes.

### 3.1. Radiocarbon ($^{14}$C)

Carbon has two naturally occurring stable isotopes, $^{12}$C (98.9%) and $^{13}$C (1.1%). In addition, a radioactive isotope of carbon ($^{14}$C, commonly known as the radiocarbon) has been extensively applied to constrain the formation timing of various carbon-containing reservoirs and systems (Dutta, 2016). In 1940, two American physicists, Martin Kamen and Sam Ruben, discovered the long-lived radioactive $^{14}$C isotope (half-life: 5730 ± 40 years) and used it as a tracer in biological systems (Elias, 2015). Later, in 1947, an American chemist Willard Libby established that plants absorb $^{14}$C in trace amounts during photosynthesis; however, this exchange stops when the plant dies (Fig. 4). Once this exchange terminates, $^{14}$C decays at its regular rate without any replacement (Fig. 4). Thus, by measuring the remaining $^{14}$C abundance in the plant material, the time elapsed since the plant died can be estimated (Libby, 1955). Libby received the Nobel Prize in Chemistry (1960) for his remarkable discovery of $^{14}$C and its applications as a chronological tool. The $^{14}$C is a cosmogenic radionuclide which is naturally produced by secondary spallation reaction of thermal neutrons from high-energy galactic and solar cosmic rays with atmospheric nitrogen. This reaction can be represented by the following equation:

$$^{14}N_7 + {}^{1}n_0 \rightarrow {}^{14}C_6 + {}^{1}p_1 \quad (1)$$

About 55% of $^{14}$C is produced in the lower stratosphere, with the remaining amount generated in the upper troposphere (Gäggeler, 1995). Based on the carbon cycle model, the global $^{14}$C production rate was estimated to be around 1.7 atoms cm$^{-2}$ s$^{-1}$ (Roth and Joos, 2013). It has been estimated that galactic cosmic rays produce around 90% of the atmospheric $^{14}$C, with the remaining amount produced by solar cosmic rays (Damon and Sternberg, 1989). The natural $^{14}$C/$^{12}$C abundance ratio of atmospheric $CO_2$ is around 1.2 × 10$^{-12}$, in equilibrium with terrestrial carbon reservoirs (Dutta, 2016). Once produced in the atmosphere, the $^{14}$C atoms rapidly oxidize to $^{14}$CO, eventually converting to $^{14}CO_2$, which gets homogenized with atmospheric $CO_2$. Ultimately, $^{14}CO_2$ gets into the terrestrial biosphere through photosynthesis in plants (Dutta, 2016). For the marine systems, $^{14}CO_2$ gets associated with the dissolved inorganic carbon through atmosphere–ocean $CO_2$ exchange. The radiocarbon dating technique does not depend on the parent ($^{14}$C) measurements to the decay product ($^{14}$N), it solely relies on the $^{14}$C

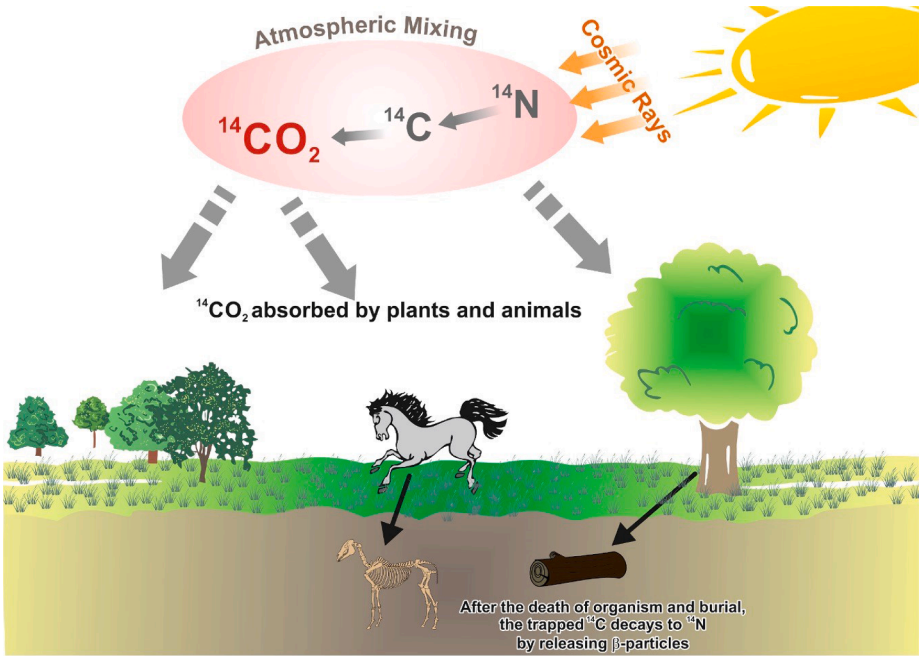


**Fig. 4.** Schematic of Radiocarbon dating wherein the cosmic rays bombard on the atmospheric nitrogen to produce $^{14}C$, which gets mixed with the $O_2$ to produce $^{14}CO_2$, which is taken by living organisms (plants and animals). The stored $^{14}C$ in the organism decays to $^{14}N$ when the organism dies and gets buried.

measurements for age estimations. However, it is important to note that the $^{14}C$ dating is based on certain prerequisites: (i) The $^{14}C$ concentration in a reservoir has remained constant throughout its age, (ii) the $^{14}C$ exchange with the ambient environment terminated after the system was closed (e.g., death of an organism), and (iii) no $^{14}C$ contamination in the sample/system from other sources(s).

The radioactive decay of radiocarbon can be expressed by the following decay equation:

$$^{14}C_6 \rightarrow {}^{14}N_7 + b^- + \overline{\upsilon} + Q \quad (2)$$

Based on the above decay equation, the radioactive $^{14}C$ decays by emission of $\beta^-$ particle, eventually producing $^{14}N$ and antineutrinos with endpoint energy (Q) of 0.156 MeV (Faure, 1986). The time elapsed since the system has stopped exchanging the atmospheric $^{14}C$ is related to initial $^{14}C$ activity ($N_0$) and final *or* contemporary $^{14}C$ activity (N). Thus, the age of the system can be estimated using the following equation:

$$t = \lambda \, In \, \frac{No}{N} \quad (3)$$

where 't' is the time elapsed since the atmospheric $^{14}C$ exchange has stopped. λ is the $^{14}C$ disintegration constant ($3.9x10^{-12}$ $sec^{-1}$; Kent, 1962).

In general, the radiocarbon ages are reported in years before present (BP), wherein the *present* represents the year 1950 CE and is considered 0 BP. The BP can represent Fraction modern (Fm) relative to modern standard or $\Delta^{14}C$ represented as per mil (‰). $\Delta^{14}C$ is the difference of $^{14}C/^{12}C$ ratio relative to the modern standard, corrected for $^{13}C$ isotopic fractionation (Stuiver and Polach, 1977).

### 3.1.1. Radiocarbon ($^{14}C$) calibration

The radiocarbon dating relies on the assumption that $^{14}C$ abundance in a reservoir is consistent through time; however, significant temporal variations in atmospheric $^{14}C$ concentrations have been reported (de Vries, 1958). Atmospheric production rates of $^{14}C$ can be linked to changes in the cosmic ray flux due to geomagnetic and heliomagnetic variabilities (de Vries effect; Dutta, 2016). For example, the solar minima period for the last century corresponds well with the higher levels of atmospheric $\Delta^{14}C$ (Fig. 5a). Due to the variation in atmospheric $^{14}C$ abundance over time, it becomes necessary to calibrate $^{14}C$ ages to get a reliable record of radiocarbon ages. Generally, the samples with known calendar ages are dated by $^{14}C$ using a Libby half-life of 5568 years (Dutta, 2016). The obtained $^{14}C$ ages ($^{14}C_B$) of samples were compared with their actual ages ($^{14}C_A$; known by other methods, e.g., dendrochronology) covering the last two millennia, yielding a relationship: $^{14}C_A = 1.4 \times {}^{14}C_B - 1100$. During 1966–1979, several $^{14}C$ calibration curves were projected but dearth of standardization ensued much confusion when the calibrated ages from different curves were compared (Klein et al., 1982). In the year 1979, a consensus calibration was established by an international working group that has updated the calibration curve on approximate intervals of 5 years. The initial $^{14}C$ calibration curve was based on a measurement of ~ 1154 samples with well-known ages covering a period of 0–8000 years BP (Klein et al., 1982). Subsequently, several improvements were made to the radiocarbon calibration curve, leading to more reliable radiocarbon ages. Initially, $^{14}C$ calibration curves were generated by closely matching the estimated dendrochronology (counting of annual growth rings of trees) based ages with radiocarbon ages of respective tree rings (Reimer et al., 2004; Stuiver, 1982; Stuiver et al., 1998a). However, the rare availability of trees with ages older than 12000 years limited the validity of $^{14}C$ calibration beyond 12000-year BP (Fairbanks et al., 2005). Thus, the $^{14}C$ calibration curves were further reinforced by accumulating composite data from various sample types: tree rings, marine varve, U-Th dated speleothem deposits, corals, and foraminifera to span the last 50000 years (Dutta, 2016). The first-time inclusion of U-Th and $^{14}C$ dated corals (Bard et al., 1993) was made in the calibration curve projected in 1993 (Reimer, 2021). Varve sediment data of the Cariaco basin (Hughen et al., 1998) was included in the calibration curve of 1998 when the data corroborated well with the Barbados coral data (Bard et al., 1998). In the calibration curve of 2004, a random walk model was incorporated to account for the uncertainties involved in $^{14}C$ ages and the calendar ages of the selected sample (Buck and Blackwell, 2004). However, IntCal04 and Marine04 calibration curves could not exceed 26 ka (Hughen et al., 2004; Reimer et al., 2004). The calibration curves Marine09 and IntCal09 proposed in 2009 were able to extend the 14C dating range to 50 kyr (Reimer et al., 2009). In 2013, the incorporation of datasets from the Bahamas and Hulu cave speleothems, terrestrial

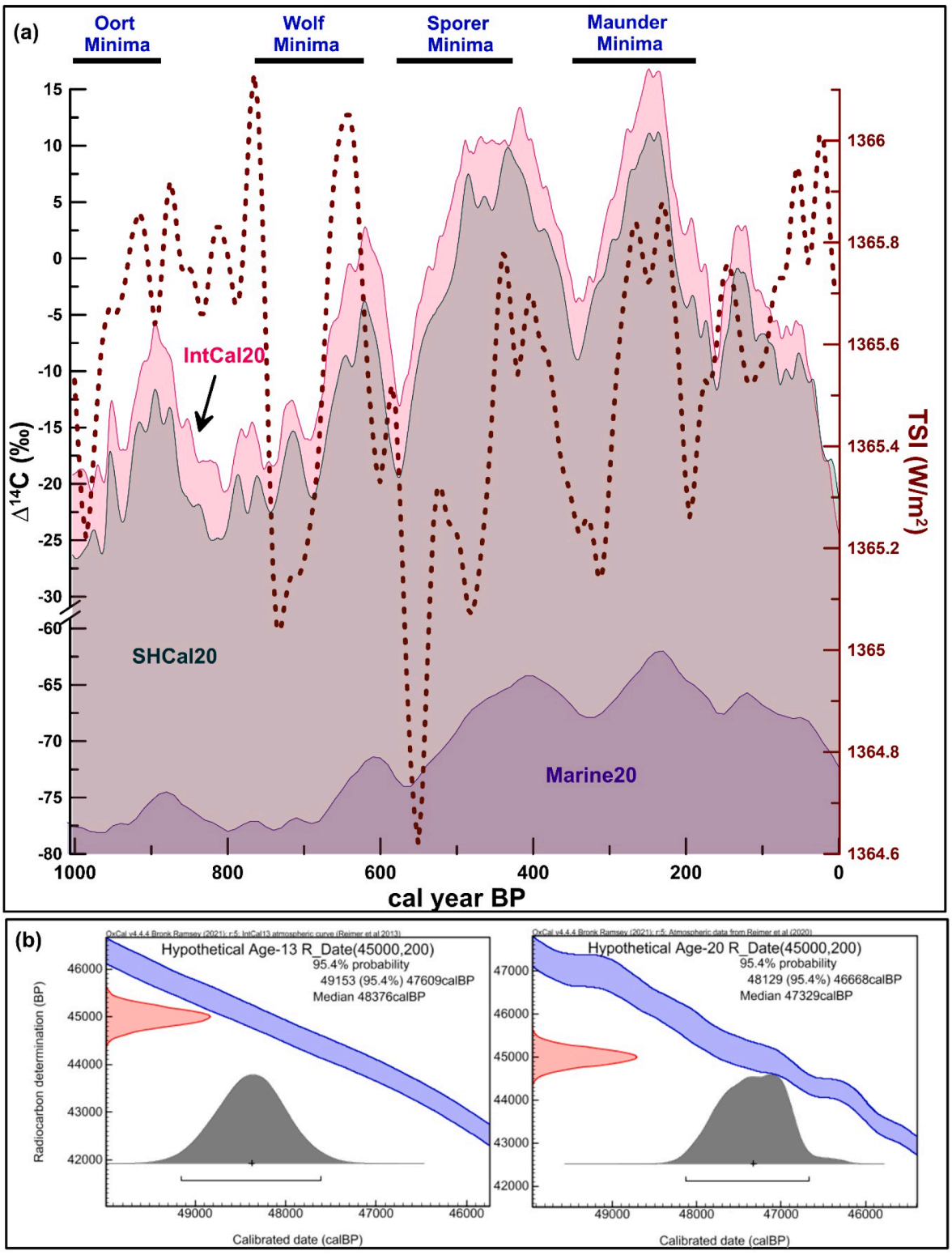


**Fig. 5.** (a) The $\Delta^{14}C$ variability from the radiocarbon calibration curves (SHCal20, IntCal20, and Marine20) and its comparison with the Total Solar Irradiance (TSI); (b) Calibration of a hypothetical $^{14}C$ age 45000 ± 200 yr BP using both IntCal13 and IntCal20 with the help of OxCal 4.4 online software which depicted ~ 1000 yr differences between the median age generated by both the calibration curves.

plant macrofossils from Japanese lake (Beck et al., 2001; Hoffmann et al., 2010; Ramsey et al., 2012; Southon et al., 2012) significantly enhanced the age range of the calibration curve of IntCal13 in comparison to the previous version IntCal09 (Reimer, 2021). The temporal resolution for Marine13 is five years until 10500-year BP. The IntCal13 and SHCal13 calibration curves are characterized by an identical temporal resolution of five years until 13800-year BP. These calibration curves demonstrate significant wiggles in $\Delta^{14}C$ on decadal to multi-decadal scales, indicating significant variations in atmospheric $^{14}C$ abundance (Dutta, 2016). The inclusion of extensive datasets and its

complicated dependency in the calendar age chronologies led to the realization that a new method with flexibility and potential to delineate the impact of specific modeling and dataset selection is the pre-requisite as the random walk method has attained its limits (Reimer, 2021). The recently proposed calibration curve of 2020 witnessed a redesigned statistical approach that utilized Bayesian splines, allowing quick execution and reliable estimation of the calibration curve than the random walk approach (Heaton et al., 2020a; Reimer, 2021). Further, instead of using a consistent offset from the atmospheric curve, the Hamburg Large Scale Geostrophic model was implemented in the marine datasets to decipher the extensive variations in the marine reservoir offsets (Butzin et al., 2020). A difference of ~ 700 years and > 1000 years are observed between the IntCal13 and IntCal20 during 34–42 kyr and 42–50 kyr, respectively which might lead to major consequences in the scientific investigation in selected studies dealing the aforementioned temporal ranges (Bard et al., 2020; Reimer, 2021). The calibration using both IntCal13 and IntCal20 (Fig. 5b) of a hypothetical $^{14}C$ age (45000 ± 200 yr BP) with the help of the OXCal v4.4.4 model was done (Hogg et al., 2013; Bronk Ramsey. 2009; Reimer, 2020; Reimer et al., 2013). The recent SHCal20 for the southern hemisphere incorporated additional tree ring data. In contrast, the period deprived of any data set from the southern hemisphere was corrected using IntCal20 with a north–south hemispheric offset model (Heaton et al., 2020b). Unlike previous versions of marine calibration curves (Marine04, Marine09, Marine13), a box model of the global carbon cycle (BICYCLE) (Kohler et al., 2006) was revised with the $CO_2$ reconstructions from ice-core records and atmospheric $\Delta^{14}C$ from IntCal20, which provided non-polar global-average marine $\Delta^{14}C$ values (Heaton et al., 2020b). A larger average offset between the ocean and the atmosphere resulting from the inclusion of the parameters used in the model is different from the previous marine curves. Thus reservoir age corrections used for regional data need to be calculated based on the Marine20 (Reimer, 2021).

### 3.1.2. *Reservoir age correction (ΔR)*

The continuous air-sea exchange of atmospheric $CO_2$ leads to a quasi-equilibrium of $^{14}C$ concentrations in DIC of surface ocean waters, with deeper layers remaining depleted in $^{14}C$. Such variations in $^{14}C$ abundances within the ocean result in surficial layers being older than the contemporary atmosphere by around 400 years (Dutta, 2016; Stuiver and Braziunas, 1993). Further, the marine organisms derive their carbon from the seawater *reservoir* with characteristic low $^{14}C/^{12}C$ ratios compared to the atmosphere, which results in older $^{14}C$ ages of marine fossils compared to terrestrial carbon samples of the same age. Generally, the spatial and temporal variabilities in ocean circulation patterns lead to a disparity in regional reservoir ages. The assessment of these regional reservoir ages is critical for the accurate and precise estimation of radiocarbon ages of marine samples (Dutta, 2016). Therefore, reservoir age correction is required on a regional scale for the necessary calibration of $^{14}C$ ages of marine samples (Stuiver et al., 1998b, 1986). At any particular time, the reservoir age correction (defined as ΔR) is estimated from the difference between the regional marine $^{14}C$ age and the global model marine $^{14}C$ age (Dutta et al., 2001; Stuiver and Braziunas, 1993). Therefore, ΔR is the value that has to be added to the global mean reservoir age (400 years) to obtain the age correction needed to offset the local reservoir effects. Lake sediments, aquatic plants, and freshwater shells are also prone to such reservoir effects. For example, a lacustrine system may receive a fractional carbon supply from a $^{14}C$ depleted source (e.g., groundwater DIC, limestone). In that case, these carbon-bearing datable materials (e.g., lake sediments, aquatic plants, and freshwater shells) can yield older ages than contemporaneous terrestrial samples (Deevey et al., 1954). Such reservoir ages can vary on scales of several hundred to more than a thousand years (Colman et al., 2000; Zoppi et al., 2001) and exhibit significant temporal fluctuations (Geyh et al., 1997). Thus, these reservoir age corrections are generally incorporated in marine and terrestrial carbon-bearing materials before calibration using MARINE20 or IntCal20 calibration curves recently introduced (Heaton et al., 2020a,b).

### 3.1.3. *Disruption of natural $^{14}C$ abundance*

Before the industrial revolution, one gram sample of fresh organic carbon underwent 13.56 ($\beta^-$) decays per minute (Vermeesch, 2014). Later, the natural atmospheric $^{14}C$ abundance was significantly modified by (i) addition of $^{14}C$ free carbon (dead carbon) to the atmosphere during the industrial era (18th to 19th century), and (ii) the addition of extra $^{14}C$ to the atmosphere during nuclear tests conducted in the 1950 s. In the following sections, we discuss some of the critical aspects that can severely impact the accuracy of radiocarbon ages.

(a) Fossil fuel produced $^{14}C$ (dead carbon).

In general, fossil fuels (e.g., coals, crude oil, natural gas) are sourced from geologically old carbon reservoirs that do not contain any radiocarbon as their ages are in millions of years. During the mid-18th century, with the advent of the Industrial revolution, coke replaced wood and charcoal as fuel for meeting growing energy demands. This led to the burning of fossil fuels (e.g., coal, crude oil, petroleum, natural gas) to meet increased energy demands. Thus, fossil fuel usage released enormous amounts of radiocarbon-free $CO_2$ into the atmosphere, eventually diluting the natural atmospheric $^{14}C$ abundance (Fergusson, 1958; Suess, 1955). Observations from $^{14}C$ measurements in tree rings suggested that the introduction of fossil-fuel $CO_2$ into the atmosphere through the industrial revolution led to a steady decrease in $\Delta^{14}C$ by 4 − 5‰ per decade during 1900–1950 (Suess, 1955). Several other tree ring records suggested a much more depletion in atmospheric $\Delta^{14}C$, from around 20 to 25‰ during the same time (Pazdur et al., 2007; Stuiver and Quay, 1981; Tans et al., 1979). This dilution of natural $^{14}C$ atmospheric abundance was termed the Suess effect (Fig. 6). Further, the disruption of natural radiocarbon by the introduction of dead radiocarbon in marine systems has also been observed. The dissolved inorganic carbon (DIC) of the global ocean indicates a decline in $\Delta^{14}C$, such as the corals from Urvina Bay, eastern equatorial Pacific Ocean, reported a Suess effect, $\Delta^{14}C$ = -6‰ during 1930–1953 (Druffel, 1981). Similarly, coral samples collected from the Cariaco Basin showed a Suess effect of $\Delta^{14}C$ = -3‰ per decade during the period 1905–1940 (Guilderson et al., 2005). Further, the $^{14}C$ analyses of mollusc shells of known ages sampled from the Arabian Sea and Bay of Bengal provided Suess effects of −3.0 ± 1.8‰ and −2.0 ± 0.5‰ per decade, respectively (Dutta, 2008). During 1900–1950, Typical marine Suess effect values of around −2 to −3‰ have been reported from most oceanic basins; however, the Suess effect of less than −1‰ has also been observed from southern great barrier reef corals (Druffel and Griffin, 1999; Dutta, 2016). Based on a global box diffusion model, a Suess effect of around −11‰ has been estimated for the duration 1880 to 1950 (-1.5‰ per decade; Stuiver et al., 1998b).

(b) Nuclear Tests produced $^{14}C$ (bomb radiocarbon).

The large-scale surficial nuclear and thermonuclear tests conducted mainly in the northern hemisphere during 1951–1963 led to a drastic disruption of atmospheric $^{14}C$ by doubling the $^{14}C/^{12}C$ ratio of the atmosphere (De Vries, 1958). These thermonuclear tests added nearly 9.1 × $10^{28}$ additional $^{14}C$ atoms to the atmosphere (Enting and Pearman, 1987; UNSCEAR, 2000). Due to this supply of extra $^{14}C$ sourced from the surficial nuclear tests, an atmospheric $\Delta^{14}C$ peak of 1000‰ was observed over the northern hemisphere in 1963 (Nydal, 1963), which exponentially declined after the signing of the Limited Nuclear Test Ban Treaty in 1963 (Dutta, 2016). The decline in atmospheric $\Delta^{14}C$ after 1963 can be explained by (i) absorption of excess $^{14}C$ by the oceanic system and terrestrial biosphere and (ii) dilution from atmospheric $^{14}C$ inventory by dead radiocarbon released by fossil fuel combustion (Levin et al., 2010). The abrupt rise in atmospheric $\Delta^{14}C$ due to extra $^{14}C$ by the

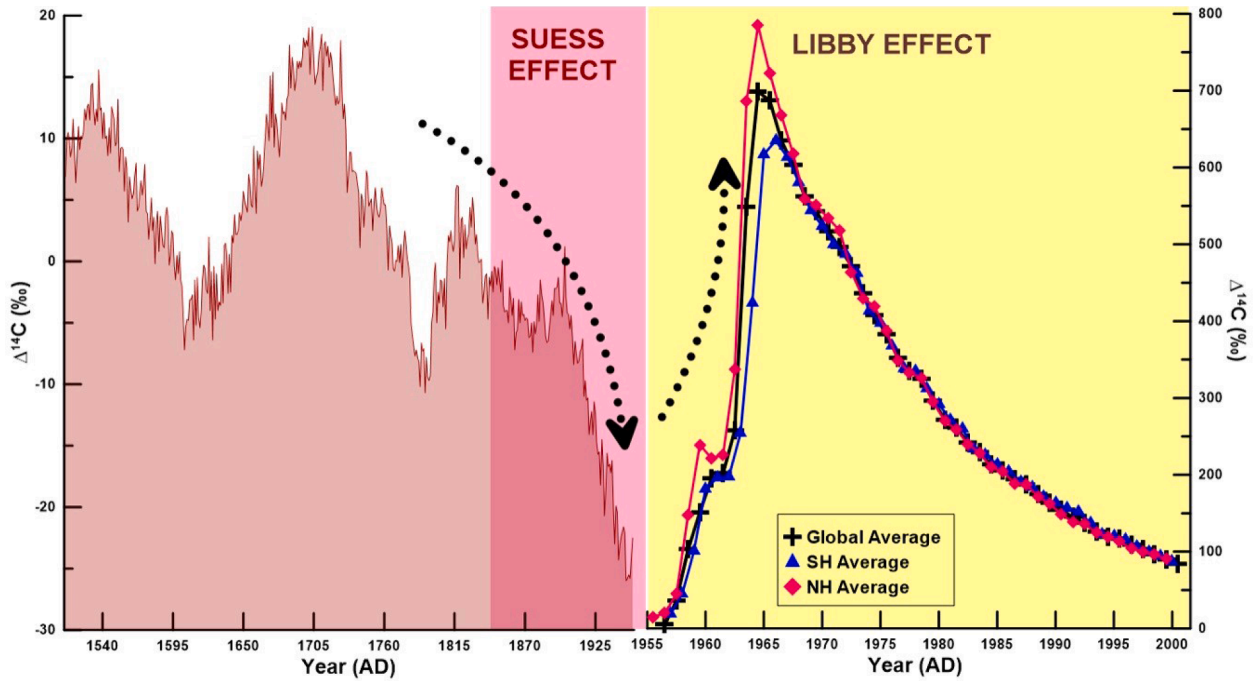


**Fig. 6.** The gradual decrease in the atmospheric $\Delta^{14}C$ after 1850 CE is caused by the dilution of anthropogenic dead carbon due to the industrial revolution termed as Suess Effect (Stuiver & Braziunas 1993). The peak of $\Delta^{14}C$ after 1950 recorded from both the hemispheres (northern and southern) and the Global average is represented, indicating the incorporation of anthropogenic $^{14}C$ into the atmosphere termed as Libby Effect.

nuclear tests has been termed the Libby effect *or* Bomb effect (Fig. 6) (Dutta, 2016). Interestingly, this significant increase in atmospheric $^{14}C$ led several researchers to use $^{14}C$ as a tracer to investigate: (i) the $CO_2$ air-sea exchange, (ii) decadal ocean circulation variability, and (iii) stratosphere-troposphere $CO_2$ exchange (Levin and Hesshaimer, 2000).

The $^{14}CO_2$ time-series data from high to mid-north latitudes suggest that a seasonal mixing of stratospheric air with elevated $\Delta^{14}C$ caused a characteristic double peak in $\Delta^{14}C$ records reaching ~ 1000‰ during August 1963 and August 1964. In the tropical regions from Debre Zeit (Bisoftu, Ethiopia), and Izana (Canary Island), respective $\Delta^{14}C$ peaks of 800‰ and 900‰ were observed (Meijer et al., 1995). A $\Delta^{14}C$ peak corresponding to 694‰ was observed from Wellington, New Zealand (Currie et al., 2011). Further, the atmospheric bomb $^{14}C$ distribution has also varied due to the seasonal migration of the Intertropical Convergence Zone (ITCZ; Hua et al., 2012; Hua and Barbetti, 2007). Due to the seasonal migration of the ITCZ and ensuing supply of southern hemispheric sourced air, the northern hemispherical regions from Ethiopia, India, Thailand, and Vietnam have recorded lower $\Delta^{14}C$ peaks than other tropical sites in Senegal and Canary Islands (Hua et al., 2012). Thus, based on seasonal migration limits of ITCZ, five hemispheric zones with similar bomb $^{14}C$ distributions (post-1950 s) were identified: Northern Hemisphere Zones 1, 2, and 3, and Southern Hemisphere Zones 1 and 2 (Hua et al., 2013). The differences in $\Delta^{14}C$ values among these zones became negligible after 1970. Further, the $\Delta^{14}C$ trends for both the hemispheres remained mostly similar till 2000. During the last decade, the global measurements of $\Delta^{14}CO2$ showed a depletion of $\Delta^{14}C$ by around 5‰ for the northern hemisphere (Graven et al., 2012; Levin et al., 2010).

The sharp gradient of the bomb atmospheric $^{14}C$ curve also serves as a tool for obtaining $^{14}C$ ages for recent organic materials (post-1950) with high accuracy of around a year to a few months (Paula J. Reimer et al., 2004). Further, in addition to its dating applications in geosciences, the application of bomb radiocarbon has been extended to other areas, such as forensic sciences (Hodge et al., 2007; Zoppi et al., 2004).

### *3.2. Beryllium-10 ($^{10}Be$) and Aluminium-26 ($^{26}Al$) isotope: Application of in-situ cosmogenic nuclides*

Solar and galactic cosmic rays enter the earth's upper atmosphere and create a cascade of secondary particles (muons and neutrons). These secondary particles bombard the mineral crystal structure embedded in crustal rocks to produce *in-situ* cosmogenic nuclides (e.g., $^{10}Be$, $^{26}Al$) on the earth's crust (Nishiizumi et al., 1989). *In-situ* cosmogenic nuclides can be classified as either radioactive (e.g., $^{10}Be$, $^{14}C$, $^{26}Al$, $^{36}Cl$) or stable (e.g., $^{3}He$, $^{21}Ne$, $^{22}Ne$). Both radioactive as well as stable *in-situ* cosmogenic nuclides can be used to study various earth surface processes (e.g., ice-sheet thinning and glacier recession rates, denudation rates, landscape evolution and development). The *in-situ* cosmogenic nuclide production in a rock is primarily caused by direct nucleon spallation reactions occurring closer to the rock's surface, decreasing exponentially with depth. For example, spallation of $^{28}Si$ and $^{16}O$ in a quartz crystal leads to the production of $^{26}Al$ and $^{10}Be$ nuclei, respectively. In deeper layers, cosmogenic nuclide production is dominated by negative muon capture and fast muon reactions (Granger and Smith, 2000). Most *in-situ* cosmogenic nuclide production is by direct nucleon spallation reactions occurring closer to the rock's surface. For example, in case of $^{10}Be$ production, it has been estimated that direct nucleon spallation reactions account for ~ 97% of the cosmogenic nuclide production. In comparison, negative muon capture and fast muon reactions contribute only around 2% and 1% of the total *in-situ* cosmogenic nuclide production, respectively (Heisinger, 1998).

#### *3.2.1. Exposure age estimation*

The application of $^{10}Be$ and $^{26}Al$ accumulation in exposure dating was initially regarded in the early 1960 s (Lal and Peters, 1967, 1962). Nevertheless, it only became possible to apply the cosmogenic nuclides to study various earth surface processes with the development of the AMS (Dorn and Phillips, 1991; Gosse and Phillips, 2001; Ivy-Ochs and Briner, 2014). The $^{10}Be$ and $^{26}Al$ abundances can be used to (i) estimate exposure ages of moraines and glacially eroded bedrocks to determine the receding rate of glaciers, and (ii) estimate *erosion* or *denudation* rates (combined physical and chemical transport rates of weathered products)

on earth's surface. In general, to determine cosmogenic radionuclide exposure ages or denudation rates in a catchment, $^{10}$Be and $^{26}$Al abundances in quartz are measured as (i) quartz is relatively resistant to weathering, (ii) quartz is found in high abundance on the earth's surface, (iii) the production rates of $^{10}$Be and $^{26}$Al in quartz are well known, (iv) production rates for $^{10}$Be and $^{26}$Al in quartz are uniform, and (v) $^{10}$Be ($T_{1/2} \sim 1.5$ Myr) and $^{26}$Al ($T_{1/2} \sim 0.7$ Myr) are radioactive and virtually non-existent in the rock *a priori*. The high abundance of quartz on the earth's surface and fair resistance of the mineral to weathering leads to minimal loss of cosmogenic radionuclides under surficial weathering. The $^{10}$Be and $^{26}$Al production rates in quartz for glacial polished granitic surfaces and landslide fields have been estimated to be $5.75 \pm 0.24$ atoms yr$^{-1}$ and $37.4 \pm 1.9$ atoms yr$^{-1}$, respectively, with a $^{26}$Al/$^{10}$Be production ratio of $\sim 6$ (Kubik et al., 1998; Nishiizumi et al., 1989).

The production rates of *in-situ* cosmogenic radionuclides in a rock exposed on the earth's surface depend on several factors. Firstly, the *in-situ* cosmogenic nuclide production rate depends on the incident cosmic ray flux and its penetration within a rock. The *in-situ* production of cosmogenic nuclide within a rock decreases exponentially with depth and can be expressed by the following relation:

$$P = P_0 \times e^{-d/A} \tag{4}$$

Here, 'P' and '$P_0$' are *in-situ* cosmogenic nuclide production rates at depth 'd' and rock surface, respectively. The 'd' is mass depth below the surface (in units of g cm$^{-2}$), which can be expressed as a product of linear depth and material density, and 'A' is the effective attenuation length of *in-situ* cosmogenic nuclide production within the rock.

Secondly, the *in-situ* cosmogenic nuclide production rate in a rock depends on its geographical location. The production rate of cosmogenic nuclides is dependent on the altitude of rock since the atmospheric shielding effect causes higher elevations to show elevated production rates. Further, spatial and temporal variability in geomagnetic field intensity can influence the incident cosmic ray flux affecting the production of cosmogenic nuclides in the rock (Desilets et al., 2006; Lal, 1991). Thirdly, land topography and coverage (e.g., by snow, foliage) can also influence the *in-situ* production rates of cosmogenic radionuclides. Since the production rate of cosmogenic nuclides diminishes with significant land cover by snow or forests, some extra correction is needed if the landscape has been shielded from the open sky (Dunne et al., 1999).

Cosmogenic nuclide abundance in a rock can be used to estimate the duration for which the rock has been exposed on the earth's surface. Thus, cosmogenic radionuclide exposure dating can help in understanding the advance and retreat of glaciers (e.g., Douglass et al., 2006). This is because glacier advances and retreats create fresh rock surfaces, which can be dated by cosmogenic radionuclides (Fig. 7). Rocks covered by a glacier on its bed undergo rapid sub-glacial erosion, which effectively removes the top layers of the glacier's bedrock. Removal of upper bedrock layers by sub-glacial erosion effectively eliminates the residual cosmogenic nuclide abundance, efficiently resetting the system. Further, there is no built-up of *in-situ* cosmogenic nuclides within the bedrock as the glacier bed is shielded from cosmic ray flux by the overlying ice layers. Similarly, any clastic fragments ("erratic" boulders carried by the glacier) removed from a dynamically eroding glacier can also be considered to have negligible initial cosmogenic nuclide abundances. Surficial exposure of glacier bedrock or clastic fragments can take place by (i) their transport to glacier's lateral margins and/or terminus and deposition as moraine during advance of the glacier, (ii) uncovering of glacially eroded clastic fragments (boulders) during the retreat of the glacier. The retreating glacier effectively exposes the bedrock, initiating the *in-situ* build-up of cosmogenic nuclides, allowing the last exposure event to be dated. Once a rock has been brought to the earth's surface by some process (e.g., glacier retreat) and exposed to cosmic rays, the cosmogenic nuclide accumulation in its surface layers occurs through the exposure duration. This principle forms the basis for dating the last exposure event by cosmogenic radionuclides. Further, upon their production in the rock, *in-situ* cosmogenic radionuclides undergo radioactive decay, depleting their abundance in the system. Any event that exposes a renewed rock surface on the earth's surface can be efficiently dated by analyzing the cosmogenic nuclide accumulation in the rock's surface, provided the production rate for the geographical location can be estimated. Once a fresh rock surface is exposed to cosmic rays, the cosmogenic nuclide ($^{10}$Be, $^{26}$Al) concentration/abundance (C; in atoms g$^{-1}$) in quartz can be expressed as:

$$C = \frac{P}{\lambda} \times \left[1 - e^{-\lambda t}\right]$$

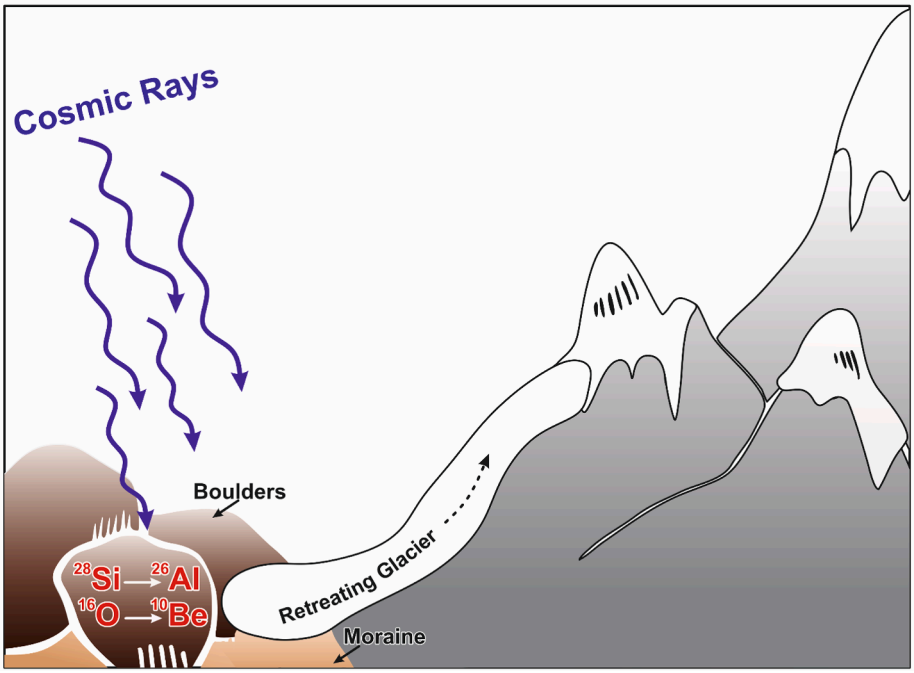


**Fig. 7.** Schematic of in-situ $^{10}$Be and $^{26}$Al production due to cosmic ray spallation on the boulders during glacier retreat.

Here, 'P' is the cosmogenic nuclide production rate (in units of atoms $g^{-1}$ $yr^{-1}$), 'λ' is the radioactive decay/disintegration constant, and 't' is the duration of exposure (in years). In general, $^{10}$Be and $^{26}$Al are commonly used to estimate the surface exposure ages and understand the timing of glacier retreat and moraine emplacements (e.g., Douglass et al., 2006). The surface exposure ages can also be estimated by measuring abundances of other *in-situ* cosmogenic nuclides: $^{3}$He, $^{14}$C, $^{21}$Ne, and $^{36}$Cl; however, $^{10}$Be and $^{26}$Al are mostly used because of better production rates estimates in quartz (Balco, 2011).

Recent developments and improvements in AMS measurement techniques during the 1980 s have significantly aided cosmogenic nuclides analyses. The increased analytical accuracy and precision using the AMS have helped understate the *in-situ* production rates of cosmogenic nuclides in rocks of known ages (e.g., Nishiizumi et al., 1989). Further, the calibration experiments performed by Lal, (1991) enabled the estimation of accurate and reliable $^{10}$Be and $^{26}$Al production rates in quartz from different altitude and latitude settings. Once these basics were established and *in-situ* cosmogenic radionuclide ($^{10}$Be, $^{26}$Al) production rates were calibrated, several studies reported cosmogenic radionuclide ages for investigating glacier chronologies to understand glacial retreats (e.g., Brook et al., 1995; Douglass et al., 2006; Glasser et al., 2011; Owen et al., 2006; Phillips et al., 1990). A comprehensive review of glacier chronology estimations using *in-situ* produced cosmogenic nuclides has been provided by Balco, (2011).

The sediment accumulation rates of the deeper ocean are crucial to decipher the climatic events witnessed by the Earth and address the oceanic material balance and budget calculations (Arrhenius, 1967; Broecker, 1971). After the production of $^{10}$Be in the atmosphere through spallation reaction on oxygen and nitrogen, the $^{10}$Be is instantaneously adsorbed on the aerosol particles and removed from the atmosphere within a year (Raisbeck et al., 1981). Consequently, $^{10}$Be is rapidly transferred to other reservoirs due to its short residence time in the atmosphere. The $^{10}$Be removal from the atmosphere occurs primarily through precipitation, consisting of $10^3$ –$10^4$ atoms/gm (Morris, 1991). In the ocean, the $^{10}$Be gets adsorbed onto the settling particles and gets scavenged to the oceanic bottom sediments resulting in the $^{10}$Be residence time of several hundred to thousands of years (Anderson et al., 1990; Raisbeck et al., 1980). The $^{10}$Be has been successfully implemented to support the deep ocean sediment cores to estimate sedimentation rates and thus can yield ages of nearly 200 kyr or beyond (Amin et al., 1975; Frank et al., 1997). With the help of $^{10}$Be, the sedimentation rates for three sediment cores from the Pacific ocean and a sediment core from the Indian ocean were estimated. Recently, a sediment core of ~ 500 cm retrieved from the equatorial Indian ocean was dated using $^{14}$C for the top ~ 60 cm. At the same time, $^{10}$Be was implemented to understand the sedimentation rates of deeper sections of the sediment core (Jena et al., 2021).

### 3.2.2. Denudation rate estimation

In addition to estimating the surface exposure ages, the *in-situ* cosmogenic nuclide abundances can also be used to evaluate denudation rates in a river catchment, provided the *in-situ* production rate of the cosmogenic nuclide in a rock is well known (Lal, 1991). If the cosmogenic nuclide production rate balances its loss via radioactive decay and erosion/denudation, the system is in a steady state. Under this scenario, the cosmogenic nuclide concentration (C; in atoms $g^{-1}$) can be expressed by the following equation (von Blanckenburg, 2005):

$$C = \frac{P_{(0)}}{\left(\lambda + \frac{\sigma\rho}{\Delta}\right)} \tag{6}$$

Here, '$P_{(0)}$' is the production rate of the cosmogenic nuclide in the mineral (in atoms $g^{-1}$ $yr^{-1}$), 'λ' is the disintegration constant of nuclide (in $yr^{-1}$), 'σ' is the denudation rate (in cm $yr^{-1}$), 'ρ' is the density of the rock (in g $cm^{-3}$), 'Δ' is the attenuation length of the cosmogenic nuclide in rock (in g $cm^{-2}$). If all the other parameters are known or can be precisely estimated, the denudation rate in a river catchment can be determined using the above equation.

The typical abundances of $^{10}$Be and $^{26}$Al are around a few thousand atoms per gram of the rock sample. Thus, in order to measure precise $^{10}$Be and $^{26}$Al abundances in the sample, (i) large sample amounts (a few grams to ~ 100 g) are taken, and (ii) measurements are done by the AMS. Prior to their mass spectrometric analysis, samples are chemically treated: any surface contaminants are removed, and Be and Al are separated and purified by chromatographic extractions.

In general, the denudation rate estimations of the entire river catchment can be done by measuring cosmogenic nuclide abundance(s) in one of these two sample types: (i) a large number of bedrock samples representing the whole catchment, and (ii) riverine sediments from a river's catchment and sub-catchments. If bedrock samples are used, it requires collecting and analyzing many representative soil and bedrock samples from various locations from the whole landscape to estimate average denudation rates in the entire river catchment. Alternatively, denudation rates on the catchment scale can be estimated by analyzing river sediments from the catchment and sub-catchments. Analyzing the river sediments to estimate denudation rates is beneficial as nature does the averaging (von Blanckenburg, 2005). On a catchment scale, the sediments collected at the outlet would provide aggregated sediments from different regions in the river upstream. Based on differences in relief, stream power, the temperature in the main channel, and small streams in the catchment and sub-catchments, the sediments derived from different regions in a catchment erode at different rates and are likely to have different cosmogenic nuclide abundances. Thus, mixing of these weathered fragments/grains and their transport within the catchment leads to averaged-out denudation rates over the catchment scale from the sediments collected at the catchment outlet. Ultimately, river sediments provide an advantage by averaging the erosion on a catchment scale and yielding denudation rates for the entire landscape contained in the catchment (e.g., Blanckenburg, 2005). Further, the application of *in-situ* cosmogenic nuclides in estimating denudation rates in a catchment depend on several assumptions: (i) there is no temporal variation in denudation rates in the catchment, i.e., the catchment is in isotopic steady-state (*in-situ* cosmogenic nuclide production is balanced by its combined removal by radioactive decay and erosion), (ii) erosion in the catchment is entirely contributed by the river, (iii) each region or sub-catchment provides the mineral quartz proportionately to regional eroding rate, (iv) the eroding rocks in the catchment have similar grain size distributions, (v) there is no quartz enrichment in sediment source area during erosion, (vi) minimal sediment storage in the drainage basin during transport, (vii) erosion timescale in the catchment is shorter than decay half-life of the cosmogenic radionuclide. These factors have been discussed in detail by von Blanckenburg, (2005) and Dosseto and Schaller, (2016). All these factors must be valid for successfully applying *in-situ* cosmogenic radionuclides in estimating catchment scale denudation rates. However, due to the complex behavior of the natural systems, it is highly possible that some of these assumptions might not be fulfilled under certain circumstances. Under such case(s), any unruly factor(s) and their impacts on calculated denudation rates must be assessed carefully (Dosseto and Schaller, 2016; von Blanckenburg, 2005).

The research in the application of cosmogenic radionuclides in estimating denudation rates on a catchment scale has been ongoing for around thirty years. In one of the earlier studies, Brown et al., (1988) measured the meteoric $^{10}$Be in river sediments to estimate denudation rates in the eastern United States. However, this study was limited by uncertainties associated with atmospheric production rates of meteoric $^{10}$Be. Subsequently, due to better constraints on their production rates, *in-situ* cosmogenic nuclides have been applied to sediments and bedrocks from various catchments to estimate spatially averaged denudation rates on a catchment scale (e.g., Brown et al., 1995; Granger et al., 1996; Kober et al., 2007; Vanacker et al., 2007). *In-situ* cosmogenic $^{26}$Al and $^{10}$Be were measured in bare bedrock surfaces on summit flats of four

western US mountain ranges (the Beartooth, Wind River, Front Range, and the Sierra Nevada) to estimate bare-bedrock erosion rates of 7.6 ± 3.9 m $Myr^{-1}$ (range: 2 to 19 m $Myr^{-1}$; Small et al., 1997). These erosion rates were within the range of previous *in-situ* cosmogenic isotope derived erosion rates from other alpine environments. By measuring the $^{10}Be/^{9}Be$ ratio in suspended sediments from the Ganga river basin, Rahaman et al., (2017) estimated a denudation rate of 140 m $Myr^{-1}$, which corresponds to a total annual sediment flux of 350 Mt, similar to sediment flux estimates derived from gauging stations (~400 Mt $y^{-1}$). The estimated denudation rate from the Ganga basin is an order of magnitude faster than typical averaged basin-wide denudation rates (~50 m $Myr^{-1}$; Saunders and Young, 1983).

## 4. Instrumental advances in Quaternary dating

### 4.1. Radiation (α, β and γ) spectroscopy: Dating recent sediments

Estimating the depositional history of recent natural archives (deposited during the last century) requires suitable dating methods that are applicable through these shorter timescales (e.g., $^{210}Pb$, $^{137}Cs$). Based on different physical and chemical properties, the short-lived radioisotope of Pb ($^{210}Pb$, $t_{1/2}$ ~ 22.3 y) can be measured using several analytical techniques (Mikalauskiene et al., 2018). The $^{210}Pb$ activity for the sediment samples can be measured by radiation (α, β or γ) spectroscopy (Jia and Torri, 2007; Lehto and Hou, 2011; Mikalauskiene et al., 2018). These measurement techniques vary in detection limits, sensitivity, reproducibility, analysis time, and dead-time between analyses (Ebaid and Khater, 2006). The $^{210}Pb$ activity estimation using γ-ray spectroscopy permits direct measurement in various natural samples, e.g., water, soil, and sediments. In contrast, the growth of its daughter, $^{210}Bi$ ($t_{1/2}$ = 5.01 day), and granddaughter, $^{210}Po$ ($t_{1/2}$ = 138.4 day), radionuclides are estimated using β and α spectroscopy, respectively. The α and $\beta^-$ spectroscopy methods assume that the parent ($^{210}Pb$) and the daughter or granddaughter radionuclides are in a secular equilibrium (Ivanovich and Harmon, 1992; Köhler et al., 2002; Swarzenski, 2013).

(a) Alpha (α) particle spectroscopy.

In the past, magnetic spectrographs were used to estimate the emission probabilities of various α-particles; however, due to their poor transmissions, longer time durations were required for spectra recordings (Aggarwal, 2019). Later, a gridded ionization chamber was introduced with an energy resolution of about 30 keV (FWHM) at 5.5 MeV (Aggarwal, 2019). In recent years, the silicon surface-barrier (SSB) and passivated implanted planar silicon (PIPS) detectors are frequently employed for α-spectroscopic investigations. Generally, the α-spectroscopy is characterized by a low background with nearly consistent detector efficiencies from 4 MeV to 9 MeV due to the short range of α-particle. Further, α- spectroscopy is relatively economical to operate and maintain relative to other mass spectrometric methods. However, α-spectroscopy method is compounded by several factors: extensive reliance on radiochemical separation, adequate source preparation, and usage of appropriate algorithms to quantify low-energy tail contribution by degradation of high energy peaks (Aggarwal, 2019).

The α particle measurement for the $^{210}Pb$ geochronometry assumes that $^{210}Pb$ and $^{210}Po$ are in secular equilibrium. Thus, $^{210}Pb$ activity and concentration can be estimated indirectly via α spectroscopy through its decay granddaughter, $^{210}Po$. The α-spectroscopy for the $^{210}Po$ measurement requires sample digestion and $^{210}Pb$ extraction from other radionuclides, followed by auto-deposition of $^{210}Po$ on metallic disc (silver, nickel, or stainless steel). Subsequently, the $^{210}Po$ activity is measured by α-spectroscopy using Silicon Surface Barrier Detector (SSBD) or Passivated Implanted Planar Silicon (PIPS) detectors (Ebaid and Khater, 2006; Vesterbacka and Ikäheimonen, 2005). Measuring $^{210}Po$ activity by α spectroscopy is a highly sensitive method with low detection limits. Ideally, the secular equilibrium is usually reached for slowly depositing undisturbed lacustrine or marine sediments. However, a secular equilibrium between $^{210}Pb$ and $^{210}Po$ activities is not attained under most natural sedimentary systems. Thus, the collected sediment samples are generally stored for at least two years (around seven $^{210}Po$ half-life) to attain a secular equilibrium between the radionuclides. In contrast to $^{210}Pb$, $^{210}Po$ is more reactive with organic matter (Cochran, 1982), resulting in the $^{210}Po$ activity enrichment in freshly deposited surface sediments. To overcome these issues, samples are generally stored for a longer time, of the order of several half-lives of $^{210}Po$ (Zaborska et al., 2007). However, to minimize the time delay, the remaining solution devoid of $^{210}Po$ obtained during sample processing should be stored for ~ 3 to 6 months to allow for $^{210}Po$ growth from the decay of $^{210}Pb$, followed by the measurement of $^{210}Po$ activity by α spectroscopy (Ebaid and Khater, 2006).

(b) Beta (β) spectroscopy.

Upon radiochemical extraction of $^{210}Pb$ from the samples, the $^{210}Pb$ measurements can be done by determining its short-lived β-emitting daughter $^{210}Bi$ ($t_{1/2}$ ~ 5.01 day). The β-particle $^{210}Bi$ measurement for $^{210}Pb$ quantification is done using the liquid scintillation counting (LSC) method. The β-spectroscopic measurement of $^{210}Pb$, unlike α-spectroscopy, does not require any sample storage for attaining secular equilibrium while yielding comparable detection limits with α-particle measurements (Villa et al., 2007). Developed in the 1950 s, the LSC technique has been extensively applied to detect and measure the activity and abundance of β-emitting radionuclides; however, it can also measure radionuclides that decay through electron capture (Hou, 2018). The absolute estimation of pure β-emitting solution through LSC was difficult due to problems arising from the precise estimation of the counting efficiency (Broda, 2003). The introduction of the triple-to-double coincidence ratio (TDCR) based LSC technique in the 1980 s allowed for efficient measurements of β-emitting and electron capture nuclides (Hou, 2018; Zimmerman et al., 2004). Moreover, the LSC technique can also perform simultaneous detection of α and β particles along with their subsequent separation (Hou, 2018; Villa et al., 2006). However, this separation is not 100% efficient, and, therefore, the α-β interferences need to be evaluated and minimized (Hou, 2018; Villa et al., 2007).

The LSC has been extensively used to measure several radionuclides: $^{210}Pb$, $^{226}Ra$, $^{228}Ra$, and $^{222}Rn$ (Mikalauskiene et al., 2018). Generally, the LSC counting efficiency for the direct estimation of $^{210}Pb$ β-particles are low and prone to sample quenching due to the low energy of the emitted β-particles. Thus, in general, to determine $^{210}Pb$ activity, the LSC based β-emission measurements are done by the $^{210}Bi$ radionuclide, which has a higher β-particle energy (Hou, 2018).

The radiochemical preparation of samples involves anion exchange column chromatography for bismuth removal from the solution. Afterward, Pb is separated from sample solutions through precipitation as sulfate ($PbSO_4$) or sulfide (PbS) and measured using the LSC (Mikalauskiene et al., 2018; Villa et al., 2007). This precipitation method for Pb separation has been recommended by several studies (Mazeika et al., 2004; Villa et al., 2007). In contrast to the α-spectrometry measurements, the major advantage of measuring $\beta^-$ particle activity using LSC is that the measurements do not need to be conducted instantly after $^{210}Pb$ separation (Lehto and Hou, 2011). The measurement of $\beta^-$ activity using LSC eliminates the sample waiting time needed for attaining the secular equilibrium as for α-spectroscopic measurements. Further, the detection limits for $\beta^-$ activity measurement using LSC are comparable to α-spectroscopy (Blanco et al., 2004) and better than γ- spectroscopy (Mikalauskiene et al., 2018). In sum, an estimated $^{210}Pb$ with β-spectroscopy has been widely applicable in different environmental samples from several locations (Jia and Torri, 2007).

(c) Gamma (γ) ray spectroscopy.

The $^{210}$Pb is frequently measured using High purity germanium (HPGe) detectors. The Germanium-based semiconductor detectors were first used for γ-ray detection and measurement in 1962 (Ewan and Tavendale, 1964). These initial detectors were flawed by p-type (Ge with acceptor impurities) or n-type (Ge with donor impurities) semiconductor materials (Khandaker and Khandaker, 2011; Knoll, 1999). Lithium is usually added to the Germanium detectors as an impurity, and through the lithium-ion drifting process, these detectors are designated as Ge(Li). The Ge(Li) detectors were commercially available from the early 1960 s to the 1980 s (Knoll, 1999). However, the Ge(Li) detectors were needed to be continuously maintained at low temperatures to function correctly. A significant achievement in the γ-ray detection was obtained with the fabrication of High Purity Germanium Detectors (HPGe) in the early 1980 s, which, unlike Ge(Li) detectors, could be kept at room temperatures (Knoll, 1999). Later, significant progress in the planar or well-type semiconductor detectors allowed the measurement of low energy (46.5 keV) photons with a high relative efficiency (Zaborska et al., 2007). $^{210}$Pb γ-ray spectroscopy in sediments is a non-destructive analytical technique, requiring negligible laboratory processing, effectively reducing the lab-based analytical work. Further, $^{210}$Pb dating also requires $^{226}$Ra activity estimation, which could be concurrently estimated with the γ-ray spectroscopy (Zaborska et al., 2007). The $^{226}$Ra activity is generally estimated by establishing the radioactive equilibrium with $^{222}$Rn followed by quantifying the intermediate daughter radionuclides $^{214}$Pb and $^{214}$Bi (Kirchener and Ehlers, 1998; Swarzenski et al., 2006). Upon attaining a secular equilibrium with its direct gaseous daughter $^{222}$Rn, the $^{226}$Ra is measured using γ-spectroscopy by measuring daughter products: $^{214}$Pb or $^{214}$Bi. While handling the sediment samples in the lab, the secular equilibrium between $^{226}$Ra and $^{222}$Rn is achieved by preventing $^{222}$Rn escape from the sample by appropriately sealing the sediment sample vial (high-density polyethylene or aluminum containers) and storing it for at least 21 days before γ-spectroscopy (Mabit et al., 2014).

The $^{210}$Pb decay by γ-rays involves the emission of low energy (46.5 keV) photons with just a 4% decay probability, and thus it involves significantly high correction factors and high relative uncertainties. Moreover, the chemical composition of the sample may also influence the self-absorption of the 46.5 keV photons (Mikalauskiene et al., 2018). Thus, $^{210}$Pb measurements for the biological and environmental samples remain challenging (Jia et al., 2006). For maximum sensitivity and accuracy for any environmental samples, generally α, or β- spectroscopy is preferred over γ-ray spectroscopy technique due to higher minimum detectable activity (MDA) for the γ-ray detector (Mabit et al., 2008).

Comparing all the three spectroscopic techniques (α, β, γ) for the $^{210}$Pb estimation suggests that the lowest MDA is achievable in α-spectroscopy while γ- spectroscopy has the highest MDA amongst the three methods. Thus, the applicability of γ- spectroscopy for the estimation of $^{210}$Pb is limited in the regions with low atmospheric deposition rates of $^{210}$Pb (Kirchner, 2011). Additionally, α and β spectroscopy needs higher sample amounts than γ spectroscopy (Ebaid and Khater, 2006; Simsek and Cagatay, 2014). The source preparation and measurements for the $^{210}$Pb using γ-spectroscopy takes nearly a day, while it takes more than ten days for $\beta^-$ spectroscopy. However, α-spectroscopy takes more time as it involves acid digestion of the samples. As an additional factor, the γ and β measurements can be immediately conducted on the samples, while for α- spectroscopic measurements, the $^{210}$Pb and $^{210}$Po need to reach their secular equilibrium before their analysis (Ebaid and Khater, 2006).

### *4.2. Accelerator mass spectrometry (AMS): Applications to cosmogenic isotopes*

The radiocarbon ($^{14}$C) dating technique is frequently used as a geochronological tool in Quaternary studies. Radiocarbon dating has significantly evolved through the latter half of the last century, aided by significant analytical, technical, and instrumental developments. During the initial development of the $^{14}$C dating method, the solid source counting technique established by Libby and associates was adopted by various radiocarbon laboratories (Libby, 1955, 1952). However, the poor efficiency and high self-absorption could only yield a maximum age of ~ 25000 years. Subsequently, to increase the radiocarbon dating range, the technique was replaced with Gas Proportional Counting (GPC) or Liquid Scintillation counting (LSC) (Cook and Van Der Plicht, 2007). The GPC and LSC techniques were recommended over the solid source counters due to the high detection efficiency (Cook and Van Der Plicht, 2007). Thus, $^{14}$C concentrations/activities were initially determined by measuring the β-decay. However, this method required more than a gram of carbon to obtain $^{14}$C ages with reasonable precision (Törnqvist et al., 2015). Later, it was realized that direct counting of $^{14}$C atoms reduces the sample size with better precision on radiocarbon ages. This became possible with the introduction and application of Accelerator Mass Spectrometry (AMS) to radiocarbon dating. This ultimately led to expansion and intensive developments and applications of radiocarbon dating to a wide array of research areas such as archaeology, oceanography, palaeoceanography, and forensics (Törnqvist et al., 2015).

Since the past decade, mass spectrometry has played a crucial role in understanding the timings of numerous processes, source and petrogenesis of various lithologies (Banerji et al., 2021; Boraiaha et al., 2020; Joshi et al., 2021b; Ray et al., 2015; Srivastava et al., 2022; Banerji et al., 2022). The significance of mass spectrometry can be understood by a combination of two characteristics: the capability to measure isotopic ratios with very high precisions and the low backgrounds in mass spectra that allow lower detection limits. In the past few decades, mass spectrometry has undergone rapid development with respect to its sensitivity, speed, and simplicity of operation (Awad et al., 2015; Joshi et al., 2021b)). Even though the isobaric interferences can hinder the performance of the mass spectrometer, but it can be taken care through the chemical purification of the element of interest.

The association of the accelerator system with the mass spectrometry setup has significantly elevated the sensitivities of selected isotopic systems, leading to the detection of rare isotopes with abundances of less than $10^{-12}$ g/g (De Laeter, 1998). The resulting mass spectrometer system: Accelerator Mass Spectrometer (AMS), has been applicable to understand the processes and timings in various earth systems: cosmosphere, atmosphere, hydrosphere, biosphere, cryosphere, technosphere, and lithosphere (Kutschera, 2013). The AMS is simply a combination of a mass spectrometer and a medium-energy accelerator that eliminates the molecular interferences at MeV energies (Jull and Burr, 2006). The AMS differs from the conventional mass spectrometry regarding the energies to which the ions are accelerated. In typical mass spectrometers, the produced ions are accelerated to energies of around thousands of volts (kV). In contrast, the ions are accelerated to millions of volts (MV) in the AMS. The higher ion energies in an AMS lead to precise detection and measurement of the atomic and molecular ions with efficient removal of isobaric interferences. Thus, we can measure the isotopic ratios for specific elements to a level of 1 in $10^{15}$ atoms (Agnihotri, 2001; Banerji, 2016). The broader acceptance of AMS in various earth science studies is due to its capability in distinguishing rare nuclides from the background, leading to the efficient measurement of nuclides with extremely low abundances (Kutschera, 2016).

The basic AMS design was first realized in 1939 when a 60-inch cyclotron was used to detect $^{3}$He at Berkeley and subsequently led to the discovery, that tritium ($^{3}$H) is radioactive, decaying to $^{3}$He by beta decay (Alvarez and Cornog, 1939; Bethe and Bacher, 1936). However, the application of AMS in quaternary dating was realized only in 1977 when the direct detection of $^{14}$C atoms with a cyclotron was attempted in positive-ion mode leading to overwhelmed flooding of positive $^{14}$N ions, masking the low abundance of $^{14}$C atoms (Muller et al., 1978; Richard et al., 1976). Subsequently, the tandem type accelerators gained impetus in the $^{14}$C detection as the carbon forms abundant negative ions while the $^{14}$N negative ions remain unstable. Additionally, the molecular

interferences at mass-14 ($^{12}CH_2^-$ and $^{13}CH^-$) were efficiently eliminated through stripping in the tandem accelerator (Hellborg et al., 2003; Purser et al., 1977). Using the AMS, the first $^{14}C$ measurements were done in the early 1980s (Purser et al., 1980). One of the most famous experiments conducted using the AMS for $^{14}C$ dating was to constrain the age of *The Shroud of Turin* (displayed at the Royal Chapel of Turin Cathedral since 1694). *The Shroud of Turin* was widely regarded as the cloth used for wrapping Jesus Christ's body after the crucifixion (Damon et al., 1989). Three different AMS laboratories (at Tucson, USA; Oxford, UK; and Zurich, Switzerland) independently tried to estimate the shroud's age using the $^{14}C$ dating. The obtained age ~691 ± 31 yr, with calibrated age ranging between 1260 CE and 1390 CE (95% confidence level), suggested that *The Shroud of Turin* belongs to the medieval times (Damon et al., 1989). Later studies recommended an interdisciplinary approach, robust protocols (Casabianca et al., 2019), the inclusion of textile analysis along with additional AMS dates fetched from the same Shroud but away from the previously sampled part (Freer-Waters and Timothy Jull, 2010). Even though the concept and age of the Shroud remained controversial due to arguable differences among the faith, historical evidence, and scientific proofs (Nicolotti, 2019), it definitely alleviated the implication of AMS in dating the antiquity.

Recently several AMS laboratories were established throughout the globe, which dominantly focus on the measurements of $^{14}C$ radionuclide for geochronological applications (Fig. 8). In addition, the AMS facility at these laboratories has also been widely utilized to determine other long-lived radionuclides, e.g., $^{10}Be$, $^{26}Al$, $^{36}Cl$, $^{41}Ca$, $^{129}I$ (Kutschera, 2013). In the last two decades, a significant breakthrough in the AMS technology was achieved with the introduction of smaller sized accelerators (Hellborg and Skog, 2008), which demonstrated acceptable performances with terminal voltages of ≤ 1 MV (Bhushan et al., 2018; Chamizo et al., 2008; Hong et al., 2010; Stan-Sion et al., 2015). Further, the coupling of gas chromatography (GC) or high-pressure liquid chromatography (HPLC) with the negative-ion gas source through the combustion stage enhanced the applicability of AMS in the biomedical field as it became possible to analyze $^{14}C$ atoms in individual organic molecules (Hughey et al., 2000). Given the half-life of $^{14}C$, the advent of AMS extended the radiocarbon dating range to around 50,000 years (Hua, 2009).

The AMS consists of five basic parts: (i) the ion source, (ii) the injection system, (iii) the accelerator, (iv) the high energy selectors, (v) and the detector (Hellborg and Skog, 2008; Tuniz et al., 1998). A Cs ion source is frequently used to produce negative ions extracted from the sample. These negative Cs ions are subsequently focussed and accelerated to energies of ~ 10–100 kV. Different accelerator types used in the AMS are cyclotrons, single-ended accelerators, linear accelerators (Tuniz et al., 1998), and tandem-type accelerators. For geochronological purposes, $^{14}C$, $^{10}Be$, and $^{26}Al$ atoms can be efficiently measured using the AMS using an accelerating potential of ~ 2–3 MV. However, other heavier isotopic systems ($^{36}Cl$ and $^{41}Ca$) are best measured using higher accelerating potentials (Jull and Burr, 2015; Purser et al., 1990, 1981). The tandem acceltarors have been a boon in the Quaternary dating techniques wherein the accelerating potential in the tandem-type accelerators increases from zero at one end to the middle and reduces back to zero at the other end. The low-energy negative ions produced from the ion source are introduced from one end of the accelerator. Subsequently, the electrons are stripped off from the molecular ions, which are then reaccelerated, emerging as high-energy positive ions from the other end of the accelerator (Jull and Burr, 2015). Further, the customized ion optics and magnets guide the selected ion masses and charge states towards the detector for measurements (Jull and Burr, 2015). The multiple AMS stages, starting with the ion source to the detectors, significantly reduce the AMS background counts (Hellborg et al., 2003). The frequently used detectors in the AMS for nuclear physics studies are gas ionization detectors, gas-filled magnets, X-ray detectors, surface barrier detectors, and time of flight detectors (Hellborg and Skog, 2008). The introduction and developments in the AMS have provided an excellent opportunity to the researchers working in earth science studies to understand various processes and their timings: air-sea $CO_2$ exchange rates, carbon sequestration, climate changes, cosmogenic isotope fluxes, denudation rate, neotectonics, geomorphology, paleoclimatology, pedology, hydrology, archaeology, and other geological and surface processes (Bhushan et al., 2019; Ivy-Ochs and Kober, 2008; Jena et al., 2022; Klein et al., 2008; Raj et al., 2022a,b).

## 5. Summary and outlook

Enforced by the continuous quest to understand the past climatic ecological and oceanographic conditions, the Quaternary dating techniques have gained significance over the last few decades. The vitality of instrumental development (e.g., AMS) in Quaternary dating is encouraging; however, improved performance and easy access for geoscientists are required. Despite significant radiometric dating developments to understand the chronology of Quaternary deposits, the qualitative and comparative methods (e.g., dendrochronology, sclerochronology, varve counting) are still used for sub-annual to decadal climate reconstruction. However, these qualitative and comparative methods are limited by their applicability in understanding certain distinct conditions. The present review has discussed a few of the frequently used radiometric dating techniques applicable in Quaternary studies. In general, the radiometric dating techniques rely on the decay of unstable radioactive isotopes, involving a disintegration constant (λ). Estimating disintegration constant with acceptable accuracy and precision can lead to further improvements in the reliability of radiometric dating methods.

The $^{210}Pb$ dating has been extensively used to provide age

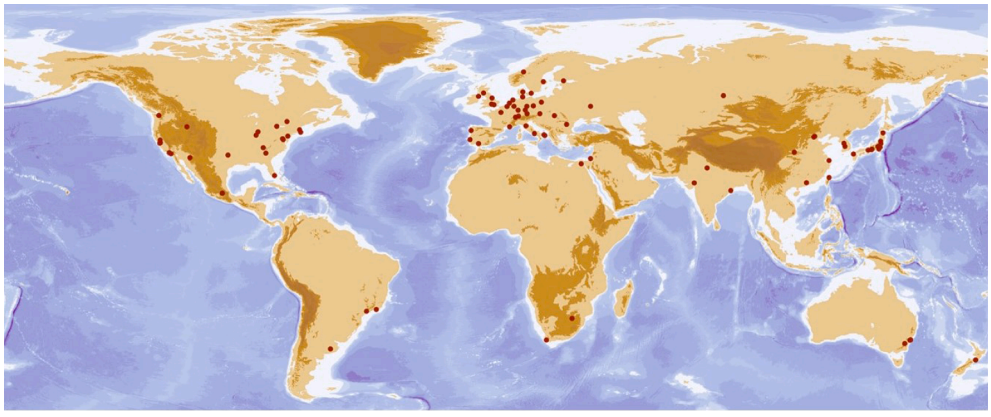

**Fig. 8.** List of Accelerator mass spectrometer (AMS) compiled by Kutschera (2013) and this study. The details of the AMS laboratories/facilities provided in the map are given in Supplementary Table S1.

constraints for sediments deposited during the last ~ 200 years (Appleby, 1997). However, sediment mixing and/or remobilization may flatten $^{210}$Pb activity with depth for surficial sedimentary layers. These factors can also significantly affect the activity of other artificial radionuclides, such as $^{137}$Cs (Appleby, 1997). Further, samples from remote and distal locations, such as deserts and polar regions with their characteristic low $^{210}$Pb atmospheric flux, have been challenging for dating by the $^{210}$Pb method (Appleby, 2008). Thus, an improved inventory of atmospheric $^{210}$Pb flux can provide a better understanding of the total $^{210}$Pb loading in these aquatic regions under consideration. Identifying and addressing various processes that cause regional variabilities in atmospheric $^{210}$Pb flux can significantly help resolve such dating issues (Appleby, 2008). In addition to $^{210}$Pb ages, $^{137}$Cs and/or other radioisotope tracers should be used to attest the reliability of the obtained ages. Further, the chemical procedures involved in α and β detection need to be simplified, and the γ detectors efficiencies need to be enhanced to establish better age controls on annual to decadal timescales.

The $^{14}$C dating has received significant attention from several paleoclimatologists due to the ubiquitous presence of carbon in natural systems and the uniformity in $^{14}$C atmospheric distribution. The transition from conventional spectroscopic method ($\beta^-$ counting) to AMS with progressive developments and improvements in the AMS has extended the $^{14}$C datable range from ~ 300 yr to a maximum of 40,000–60,000 yr. Paleoceanographic and paleoclimatic reconstruction for the late Quaternary Period is incomplete without the AMS ages on the organic sediment fraction and/or marine foraminifera shells (Banerji et al., 2020; Banerji and Padmalal, 2022; Haridas et al., 2022). Even though the AMS is an irreplacable tool, under unavoidable circumstances it can also yield reverse ages which restricts the paleoclimatic interpretations (Banerji et al., 2020; Shaji et al., 2022). Despite significant efforts made in instrumental developments in AMS, the applicability of $^{14}$C for samples from the last few centuries remain infirm due to deviation in natural $^{14}$C abundance caused by the anthropogenic intervention (Loutre, 2009). Although atmospheric $^{14}$C distribution is assumed to have remained constant in the past (before the industrial era), significant fluctuations in atmospheric $^{14}$C distribution have been reported primarily due to instabilities in the solar and galactic cosmic ray flux (Stuiver and Braziunas, 1989). Further, the variability in solar flux through time has significant implications for climatic perturbations (Bradley, 2015). Thus, the $^{14}$C ages are calibrated (using models, e.g., IntCal20 and SHCal20) for natural archives and ΔR reservoir age corrections for marine samples are made for reducing the uncertainties caused by natural variability in the atmospheric $^{14}$C distribution (Dutta, 2016). However, an improved temporal resolution for the $^{14}$C calibration curve and a better understanding and increased datasets of the marine reservoir ages are needed to yield accurate and reliable radiocarbon ages for geological and archaeological samples. The incorporation of the dataset in the calibration curves might eventually provide location-specific calibration curves and thereby improve the accuracy and precision of the estimated radiocarbon ages (Heaton et al., 2020a, b).

The *in-situ* cosmogenic radionuclide dating of fresh rock surfaces produced by glacial retreat has made a significant impact in understanding the glacier dynamics, and the obtained information is of great importance to glacier geoscientists. The application of *in-situ* cosmogenic radionuclides has led to significant contributions in understanding the timing of glacier retreat and hence helped in addressing the glacier chronology. This has been extremely helpful in comprehending the impact of changing climate on the retreat of glaciers. In particular, the application of *in-situ* cosmogenic radionuclides has been a lucrative approach in delineating the glacier chronology in cases where other dating method can fails to yield reliable ages. Further, *in-situ* cosmogenic nuclides can help in understanding the spatially averaged denudation rates in a river's catchment. This can be advantageous in assessing the weathering and erosion processes within a particular landscape. In general, the catchment-wide denudation rates are investigated using the *in-situ* cosmogenic radionuclides, mostly analyzing the quartz extracted from alluvial sediments or weathered debris. Depending on the rate of denudation and cosmogenic radionuclide used (e.g., $^{10}$Be, $^{26}$Al), these denudation rates can be estimated for integrated timescales of $10^3$ to $10^5$ years. Thus, the application of *in-situ* cosmogenic radionuclides provide cues on the denudation rates over a landscape that can help in establishing a relatively long-term record of the weathering and erosion on a catchment scale. The last few decades have witnessed increased usage of *in-situ* cosmogenic radionuclides in addressing the denudation rates, primarily due to significant developments and refinements in the AMS. In the last decade, complex surface exposure dating instigated the applicability of coupled *in-situ* $^{14}$C-$^{10}$Be measurements in quartz mineral (Hippe, 2017; Muzikar, 2020). Despite the fact that the *in-situ* $^{14}$C measurement protocols in the quartz were established in the 1990 s (Jull et al., 1992; Lifton et al., 2001), its extraction from the terrestrial rocks has been a daunting task (Hippe, 2017) and thus has been employed in limited studies on glacial landscape (Fogwill et al., 2014; Miller et al., 2006; White et al., 2011) and chronometric investigation of sediment routing and sediment storage in fluvial system (Hippe et al., 2012; Wittmann and von Blanckenburg, 2009) and to infer the rapid surface erosion events (Mudd, 2017). However, with only limited studies, the utility of coupled *in-situ* $^{14}$C-$^{10}$Be remains largely unexplored, but has a huge scope to provide chronologies to the complex surface exposures for the late Quaternary Period specifically the late Pleistocene to Holocene (Hippe, 2017).

The areas of instrumental development and the Quaternary dating techniques are closely knitted and the future of Quaternary studies relies on the improvement of dating accuracy and precision. Thus, conjoint progression in science and technology is the prerequisite for the quantum leap in the geochronological studies in Earth Sciences, particularly for the Quaternary timeframe.

## Declaration of Competing Interest

The authors declare that they have no known competing financial interests or personal relationships that could have appeared to influence the work reported in this paper.

## Acknowledgments

USB and KBJ are thankful to Director NCESS for his constant encouragement. USB is grateful to Prof. Ravi Bhushan for instilling the fundamentals of Quaternary dating techniques and Dr. D. Padmalal for his constant support and encouragement. Authors are thankful to the Co-Editor-in-Chief, Dr. Vineet Gahalaut. Authors are grateful to the reviewer, Prof. A.J.T Jull for his constructive comments and suggestions that significantly improvised the manuscript. Authors are thankful to Dr. Ravi Shankar for proof-reading the manuscript. We have tried to incorporate most of the related research contributions and if any of the relevant studies has been missed in this review paper, it was unintentional.

## Appendix A. Supplementary data

Supplementary data to this article can be found online at https://doi.org/10.1016/j.jaesx.2022.100091.

## References

Abril Hernández, J.-M., 2016. A $^{210}$Pb-based chronological model for recent sediments with random entries of mass and activities: Model development. J. Environ. Radioact. 151, 64–74. https://doi.org/10.1016/j.jenvrad.2015.09.018.

Aggarwal, S.K., 2019. Analytical Methods of alpha emitting isotopes in nuclear. https://doi.org/10.1039/C6AY00920D.

Agnihotri, R., 2001. Chemical and Isotopic studies of sediments from Arabian Sea and Bay of Bengal. Mohanlal Sukhadia University, Udaipur, Faculty of Science.

Alexander, C.R., Lee, H.J., 2009. Sediment accumulation on the Southern California Bight continental margin during the twentieth century, in: Lee, H.J., Normark, W.R. (Eds.), Geological Society of America Special Paper. pp. 69–87.

Alley, R.B., 2004. GISP2 ice core temperature and accumulation data. IGBP PAGES/World Data Cent. Paleoclimatology Data Contrib, Ser, p. 13.

Alvarez, L.W., Cornog, R., 1939. Helium and hydrogen of mass 3. Phys. Rev. 56 (6), 613.

Amin, B.S., Lal, D., Somayajulu, B.L.K., 1975. Chronology of marine sediments using the 10Be method: intercomparison with other methods. Geochim. Cosmochim. Acta 39 (8), 1187–1192. https://doi.org/10.1016/0016-7037(75)90060-5.

Andersen, T.J., 2017. Some practical considerations regarding the application of $^{210}$Pb and $^{137}$Cs dating to estuarine sediments. Applications of Paleoenvironmental Techniques in Estuarine Studies. 121–140.

Anderson, R.F., Lao, Y., Broecker, W.S., Trumbore, S.E., Hofmann, H.J., Wolfli, W., 1990. Boundary scavenging in the Pacific Ocean: a comparison of $^{10}$Be and $^{231}$Pa. Earth Planet. Sci. Lett. 96 (3–4), 287–304. https://doi.org/10.1016/0012-821X(90)90008-L.

Anspaugh, L.R., Catlin, R.J., Goldman, M., 1988. The global impact of the Chernobyl reactor accident. Science (80-.) 242 (4885), 1513–1519.

Aoyama, M., Hirose, K., Suzuki, Y., Inoue, H., Sugimura, Y., 1986. High level radioactive nuclides in Japan in May. Nat. 321 (6073), 819–820.

Appleby, P.G., 2008. Three decades of dating recent sediments by fallout radionuclides: a review. The Holocene 18 (1), 83–93. https://doi.org/10.1177/0959683607085598.

Appleby, P.G., 2001. Tracking Environmental Change Using Lake Sediments-Developments in Paleoenvironmental Research. Springer, Dordrecht. https://doi.org/10.1007/0-306-47669-X_9.

Appleby, P.G., 1997. Dating recent sediments by $^{210}$Pb: Problems and solutions, in: Proc. 2nd NKS/EKO-1 Seminar, Helsinki. pp. 7–24.

Appleby, P.G., Oldfield, F., 1992. Applications of lead-210 to sedimentation studies, in: Uranium-Series Disequilibrium: Applications to Earth, Marine, and Environmental Sciences. 2. Ed. pp. 731–778.

Appleby, P.G., Oldfield, F., 1978. The calculation of lead-210 dates assuming a constant rate of supply of unsupported $^{210}$Pb to the sediment. Catena 5 (1), 1–8. https://doi.org/10.1016/S0341-8162(78)80002-2.

Arias-Ortiz, A., Masqué, P., Garcia-Orellana, J., Serrano, O., Mazarrasa, I., Marbá, N., Lovelock, C.E., Lavery, P.S., Duarte, C.M., 2018. Reviews and syntheses: $^{210}$Pb-derived sediment and carbon accumulation rates in vegetated coastal ecosystems - Setting the record straight. Biogeosciences 15, 6791–6818. https://doi.org/10.5194/bg-15-6791-2018.

Arrhenius, G., 1967. Deep sea sedimentation: a critical review of US work. Trans. Am. Geophys. Union 48, 604–631.

Awad, H., Khamis, M.M., El-Aneed, A., 2015. Mass spectrometry, review of the basics: Ionization. Appl. Spectrosc. Rev. 50, 158–175. https://doi.org/10.1080/05704928.2014.954046.

Balco, G., 2011. Contributions and unrealized potential contributions of cosmogenic-nuclide exposure dating to glacier chronology, 1990–2010. Quat. Sci. Rev. 30, 3–27. https://doi.org/10.1016/j.quascirev.2010.11.003.

Baloga, V., Kholoscha, V., 2006. National report of Ukraine. Twenty Years after Chornobyl Accid. Futur. Outlook.

Banerji, U.S., 2016. Holocene climatic variability using mudflats from Saurashtra western india. Maharaja Sahyajirao University of Baroda. https://doi.org/http://hdl.handle.net/10603/161430.

Banerji, U.S., Dubey, C.P, Goswami, V., Joshi, K.B., 2022. Geochemical indicators inprovenance estimation. In: Armstrong-Altrin, John S., Pandarinath, Kailasa, Verma, Sanjeet Kumar (Eds.), Geochem. Treas. Petrogen. Process. Springer Nature.

Banerji, U.S., Arulbalaji, P., Padmalal, D., 2020. Holocene climate variability and Indian Summer Monsoon: An overview. Holocene 30, 744–773. https://doi.org/10.1177/0959683619895577.

Banerji, U.S., Bhushan, R., Joshi, K.B., Shaji, J., Jull, A.J.T., 2021. Hydroclimate variability during the last two millennia from the mudflats of Diu Island, Western India. Geol. J. 3584–3604. https://doi.org/10.1002/gj.4116.

Banerji, U.S., Bhushan, R., Jull, A.J.T., 2019. Signatures of global climatic events and forcing factors for the last two millennia on the active mudflats of Rohisa, southern Saurashtra, Gujarat, western India. Quaternary International 507, 172–187. https://doi.org/10.1016/j.quaint.2019.02.015.

Banerji, U.S., Padmalal, D., 2022. Bond events and monsoon variability during Holocene-Evidence from marine and continental archives. In: Kumaran, K.P.N., Padmalal, D. (Eds.), Holocene Climate Change and Environment. Elsevier Inc, pp. 293–338. https://doi.org/10.1016/B978-0-323-90085-0.00016-4.

Banner, J.L., 2004. Radiogenic isotopes: Systematics and applications to earth surface processes and chemical stratigraphy. Earth-Science Rev. 65 (3-4), 141–194. https://doi.org/10.1016/S0012-8252(03)00086-2.

Bard, E., Arnold, M., Fairbanks, R.G., Hamelin, B., 1993. $^{230}$Th-$^{234}$U and $^{14}$C ages obtained by mass spectrometry on corals. Radiocarbon 35 (1), 191–199. https://doi.org/10.1017/S0033822200013886.

Bard, E., Arnold, M., Hamelin, B., Tisnerat-Laborde, N., Cabioch, G., 1998. Radiocarbon calibration by means of mass spectrometric $^{230}$Th/$^{234}$U and $^{14}$C ages of corals: An updated database including samples from Barbados, Mururoa and Tahiti. Radiocarbon 40 (3), 1085–1092. https://doi.org/10.1017/S0033822200019135.

Bard, E., Heaton, T.J., Talamo, S., Kromer, B., Reimer, R.W., Reimer, P.J., 2020. Extended dilation of the radiocarbon time scale between 40,000 and 48,000 y BP and the overlap between Neanderthals and Homo sapiens. Proc. Natl. Acad. Sci. USA 117 (35), 21005–21007. https://doi.org/10.1073/pnas.2012307117.

Barsanti, M., Garcia-Tenorio, R., Schirone, A., Rozmaric, M., Ruiz-Fernández, A.C., Sanchez-Cabeza, J.A., Delbono, I., Conte, F., De Oliveira Godoy, J.M., Heijnis, H., Eriksson, M., Hatje, V., Laissaoui, A., Nguyen, H.Q., Okuku, E., Al-Rousan, S.A., Uddin, S., Yii, M.W., Osvath, I., 2020. Challenges and limitations of the $^{210}$Pb sediment dating method: Results from an IAEA modelling interlaboratory comparison exercise. Quat. Geochronol. 59 https://doi.org/10.1016/j.quageo.2020.101093.

Beck, J.W., Richards, D.A., Lawrence, R., Edwards, Silverman, B.W., Smart, P.L., Donahue, D.J., Hererra-Osterheld, S., Burr, G.S., Calsoyas, L., Timothy, A.J., Jull, Biddulph, D., 2001. Extremely large variations of atmospheric $^{14}$C concentration during the last glacial period. Science 292 (80), 2453–2458.

Bethe, H.A., Bacher, R.F., 1936. Nuclear physics A. Stationary states of nuclei. Rev. Mod. Phys. 8 (2), 82–229.

Bhushan, R., Yadava, M.G., Shah, M.S., Banerji, U.S., Raj, H., Shah, C., Dabhi, A.J., 2019. First results from the PRL Accelerator Mass Spectrometer. Curr. Sci. 116, 361–363.

Bhushan, R., Yadava, M.G., Shah, M.S., Raj, H., 2018. Performance of a new 1MV AMS facility (AURiS) at PRL, Ahmedabad, India. Nucl. Instruments Methods Phys. Res. Sect. B Beam Interact. with Mater. Atoms 439, 76–79. https://doi.org/10.1016/j.nimb.2018.12.003.

Blanco, P., Lozano, J.C., Gómez Escobar, V., Vera Tomé, F., 2004. A simple method for $^{210}$Pb determination in geological samples by liquid scintillation counting. Appl. Radiat. Isot. 60 (1), 83–88. https://doi.org/10.1016/j.apradiso.2003.09.011.

Boraiaha, C.K., Joshi, K.B., Kerr, A.C., Padhi, J.K., Mishra, S.S., Chandan, R., 2020. Field, petrographic and geochemical characteristics of Sullya alkaline complex in the Cauvery Shear Zone (CSZ), southern India: Implications for petrogenesis. J. Earth Syst. Sci. 129 https://doi.org/10.1007/s12040-020-1369-1.

Bradley, R.S., 2015. Dating Methods I. In: Paleoclimatology. Elsevier, pp. 55–101. https://doi.org/10.1016/B978-0-12-386913-5.00003-X.

Breithaupt, J.L., Smoak, J.M., Smith, T.J., Sanders, C.J., 2014. Temporal variability of carbon and nutrient burial, sediment accretion, and mass accumulation over the past century in a carbonate platform mangrove forest of the Florida Everglades. J. Geophys. Res. Biogeosciences 119 (10), 2032–2048.

Broda, R., 2003. A review of the triple-to-double coincidence ratio (TDCR) method for standardizing radionuclides. Appl. Radiat. Isot. 58 (5), 585–594. https://doi.org/10.1016/S0969-8043(03)00056-3.

Broecker, W.S., 1971. Calcite accumulation rates and glacial to interglacial changes in oceanic mixing. In: Turekian, K.K. (Ed.), Late Cenozoic Glacial Ages. Yale University Press, pp. 239–265.

Brook, E.J., Kurz, M.D., Ackert, R.P., Raisbeck, G., Yiou, F., 1995. Cosmogenic nuclide exposure ages and glacial history of late Quaternary Ross Sea drift in McMurdo Sound. Antarctica. Earth Planet. Sci. Lett. 131, 41–56. https://doi.org/10.1016/0012-821X(95)00006-X.

Brown, E.T., Stallard, R.F., Larsen, M.C., Raisbeck, G.M., Yiou, F., 1995. Denudation rates determined from the accumulation of in situ-produced $^{10}$Be in the luquillo experimental forest. Puerto Rico. Earth Planet. Sci. Lett. 129, 193–202. https://doi.org/10.1016/0012-821X(94)00249-X.

Brown, L., Pavich, M.J., Hickman, R.E., Klein, J., Middleton, R., 1988. Erosion of the eastern United States observed with $^{10}$Be. Earth Surf. Process. Landforms 13 (5), 441–457. https://doi.org/10.1002/esp.3290130509.

Buck, C.E., Blackwell, P.G., 2004. Formal statistical models for estimating radiocarbon calibration curves. Radiocarbon 46 (3), 1093–1102. https://doi.org/10.1017/S0033822200033026.

Buesseler, K.O., 1997. The isotopic signature of fallout plutonium in the North Pacific. J. Environ. Radioact. 36 (1), 69–83. https://doi.org/10.1016/S0265-931X(96)00071-9.

Butler, D., 2011. Radioactivity spreads in Japan. Nature 471 (7340), 555–556.

Butzin, M., Heaton, T.J., Köhler, P., Lohmann, G., 2020. A Short Note on Marine Reservoir Age Simulations Used in IntCal20. Radiocarbon 62 (4), 865–871. https://doi.org/10.1017/RDC.2020.9.

Callaway, J.C., DeLaune, R.D., Patrick, W.H., 1996. Chernobyl $^{137}$Cs used to determine sediment accretion rates at selected northern European coastal wetlands. Limnol. Oceanogr. 41 (3), 444–450. https://doi.org/10.4319/lo.1996.41.3.0444.

Casabianca, T., Marinelli, E., Pernagallo, G., Torrisi, B., 2019. Radiocarbon Dating of the Turin Shroud: New Evidence from Raw Data. Archaeometry 61 (5), 1223–1231. https://doi.org/10.1111/arcm.12467.

Chamizo, E., López-Gutiérrez, J.M., Ruiz-Gómez, A., Santos, F.J., García-León, M., Maden, C., Alfimov, V., 2008. Status of the compact 1 MV AMS facility at the Centro Nacional de Aceleradores (Spain). Nucl. Instruments Methods Phys. Res. Sect. B Beam Interact. with Mater. Atoms 266 (10), 2217–2220. https://doi.org/10.1016/j.nimb.2008.02.061.

Chino, M., Nakayama, H., Nagai, H., Terada, H., Katata, G., Yamazawa, H., 2011. Preliminary Estimation of Release Amounts of $^{131}$I and $^{137}$Cs Accidentally Discharged from the Fukushima Daiichi Nuclear Power Plant into the Atmosphere. J. Nucl. Sci. Technol. 48 (7), 1129–1134. https://doi.org/10.1080/18811248.2011.9711799.

Cochran, J.K., 1982. The oceanic chemistry of the U-and Th-series nuclides, in: Uranium Series Disequilibrium: Applications to Environmental Problems.

Colman, S.M., King, J.W., Jones, G.A., Reynolds, R.L., Bothner, M.H., 2000. Holocene and recent sediment accumulation rates in Southern Lake Michigan. Quat. Sci. Rev. https://doi.org/10.1016/S0277-3791(00)00007-X.

Cook, G.T., Van Der Plicht, J., 2007. Radiocarbon dating | Conventional method. Encyclopedia of Quaternary Science. 2899–2911. https://doi.org/10.1016/B0-44-452747-8/00040-5.

Crawford, A.R., 1970. The Precambrian geochronology of Rajasthan and Bundelkhand, northern India. Can. J. Earth Sci. 7 (1), 91–110.

Crozaz, G., Picciotto, E., De Breuck, W., 1964. Antarctic snow chronology with Pb 210. J. Geophys. Res. 69 (12), 2597–2604. https://doi.org/10.1029/jz069i012p02597.

Currie, K.I., Brailsford, G., Nichol, S., Gomez, A., Sparks, R., Lassey, K.R., Riedel, K., 2011. Tropospheric $^{14}CO_2$ at Wellington. Biogeochemistry 104 (1–3), 5–22. https://doi.org/10.1007/s10533-009-9352-6.

Damon, P.E., Donahue, D.J., Gore, B.H., Hatheway, A.L., Jull, A.J.T., Linick, T.W., Sercel, P.J., Toolin, L.J., Bronk, C.R., Hall, E.T., Hedges, R.E.M., Housley, R., Law, I. A., Perry, C., Bonani, G., Trumbore, S., Woelfli, W., Ambers, J.C., Bowman, S.G.E., Leese, M.N., Tite, M.S., 1989. Radiocarbon dating of the Shroud of Turin. Nature 337 (6208), 611–615. https://doi.org/10.1038/337611a0.

Damon, P.E., Sternberg, R.E., 1989. Global Production and Decay of Radiocarbon. Radiocarbon 31 (03), 697–703.

De Laeter, J.R., 1998. Mass spectrometry and geochronology. Mass Spectrom. Rev. 17, 97–125. https://doi.org/10.1002/(SICI)1098-2787(1998)17:2<97::AID-MAS2>3.0.CO;2-J.

De Vries, H., 1958a. Variation in concentration of radiocarbon with time and location on earth. Proc. Koninkl. Nederl. Akad. Wet. B 61, 1–9.

Vries, H. De, 1958b. Atomic bomb effect: variation of radiocarbon in plants, shells, and snails in the past 4 years. Science 128, 250–251. doi:10.1126/science.128.3318.250.

Deevey, E.S., Gross, M.S., Hutchinson, G.E., Kraybill, H.L., 1954. The natural C14 contents of materials from hard-water lakes. Proc. Natl. Acad. Sci. 40 (5), 285–288. https://doi.org/10.1073/pnas.40.5.285.

Desilets, D., Zreda, M., Prabu, T., 2006. Extended scaling factors for in situ cosmogenic nuclides: New measurements at low latitude. Earth Planet. Sci. Lett. 246, 265–276. https://doi.org/10.1016/j.epsl.2006.03.051.

Dorn, R.I., Phillips, F.M., 1991. Surface exposure dating: Review and critical evaluation. Phys. Geogr. 12 (4), 303–333. https://doi.org/10.1080/02723646.1991.10642436.

Dosseto, A., Schaller, M., 2016. The erosion response to Quaternary climate change quantified using uranium isotopes and in situ-produced cosmogenic nuclides. Earth-Science Rev. 155, 60–81. https://doi.org/10.1016/j.earscirev.2016.01.015.

Douglass, D.C., Singer, B.S., Kaplan, M.R., Mickelson, D.M., Caffee, M.W., 2006. Cosmogenic nuclide surface exposure dating of boulders on last-glacial and late-glacial moraines, Lago Buenos Aires, Argentina: Interpretive strategies and paleoclimate implications. Quat. Geochronol. 1, 43–58. https://doi.org/10.1016/j.quageo.2006.06.001.

Druffel, E.M., 1981. Radiocarbon in annual coral rings from the eastern tropical Pacific Ocean. Geophys. Res. Lett. 8 (1), 59–62.

Druffel, E.R.M., Griffin, S., 1999. Variability of surface ocean radiocarbon and stable isotopes in the southwestern Pacific. J. Geophys. Res. Ocean. 104 (C10), 23607–23613.

Dunne, J., Elmore, D., Muzikar, P., 1999. Scaling factors for the rates of production of cosmogenic nuclides for geometric shielding and attenuation at depth on sloped surfaces. Geomorphology 27, 3–11. https://doi.org/10.1016/S0169-555X(98)00086-5.

Dutta, K., 2016. Sun, Ocean, Nuclear Bombs, and Fossil Fuels: Radiocarbon Variations and Implications for High-Resolution Dating. Annu. Rev. Earth Planet. Sci. 44 (1), 239–275. https://doi.org/10.1146/annurev-earth-060115-012333.

Dutta, K., 2008. Marine $^{14}$C Reservoir Age and Suess Effect in the Indian Ocean. e-Journal Earth Sci. India 1, 175–188.

Dutta, K., Bhushan, R., Somayajulu, B.L.K., 2001. ΔR correction values for the northern Indian Ocean. Radiocarbon 43, 483–488. https://doi.org/10.1017/S0033822200038376.

Ebaid, Y.Y., Khater, A.E.M., 2006. Determination of $^{210}$Pb in environmental samples. J. Radioanal. Nucl. Chem. 270 (3), 609–619. https://doi.org/10.1007/s10967-006-0470-5.

Elias, S.A., 2015. Reference Module in Earth Systems and Environmental Sciences. Elsevier.

Emiliani, C., 1955. Pleistocene Temperatures. J. Geol. 63 (6), 538–578. https://doi.org/10.1086/626295.

Enting, I.G., Pearman, G.I., 1987. Description of a one-dimensional carbon cycle model calibrated using techniques of constrained inversion. Tellus B 39 B, 459–476. https://doi.org/10.1111/j.1600-0889.1987.tb00206.x.

Ewan, G.T., Tavendale, A.J., 1964. High-Resolution Studies of Gamma-Ray Spectra Using Lithium-Drift Germanium Gamma-Ray Spectrometers. Can. J. Phys. 42 (11), 2286–2331. https://doi.org/10.1139/p64-208.

Fairbanks, R.G., Mortlock, R.A., Chiu, T.-C., Cao, L.i., Kaplan, A., Guilderson, T.P., Fairbanks, T.W., Bloom, A.L., Grootes, P.M., Nadeau, M.J., 2005. Radiocarbon calibration curve spanning 0 to 50,000 years BP based on paired $^{230}$Th/$^{234}$U/$^{238}$U and $^{14}$C dates on pristine corals. Quat. Sci. Rev. 24 (16–17), 1781–1796. https://doi.org/10.1016/j.quascirev.2005.04.007.

Faure, G., 1986. Principles of isotope geology. Second edition, John Wiley Sons.

Fergusson, G.J., 1958. Reduction of atmospheric radiocarbon concentration by fossil fuel carbon dioxide and the mean life of carbon dioxide in the atmosphere. Proc. R. Soc. London. Ser. A. Math. Phys. Sci. 243, 561–574. https://doi.org/10.1098/rspa.1958.0021.

Fogwill, C.J., Turney, C.S.M., Golledge, N.R., Rood, D.H., Hippe, K., Wacker, L., Wieler, R., Rainsley, E.B., Jones, R.S., 2014. Drivers of abrupt Holocene shifts in West Antarctic ice stream direction determined from combined ice sheet modelling and geologic signatures. Antarct. Sci. 26 (6), 674–686. https://doi.org/10.1017/S0954102014000613.

Frank, M., Schwarz, B., Baumann, S., Kubik, P.W., Suter, M., Mangini, A., 1997. A 200 kyr record of cosmogenic radionuclide production rate and geomagnetic field intensity from 10Be in globally stacked deep-sea sediments. Earth Planet. Sci. Lett. 149 (1-4), 121–129.

Freer-Waters, R.A., Timothy Jull, A.J., 2010. Investigating a dated piece of the Shroud of Turin. Radiocarbon 52 (4), 1521–1527. https://doi.org/10.1017/S0033822200056277.

Gäggeler, H.W., 1995. Radioactivity in the atmosphere. Radiochim. Acta 70-71 (Supplement), 345–354.

Garcia, A., 1980. Global distribution of $^{137}$Cs inputs for soil erosion and sedimentation studies. No. IAEA-TECDOC–1028 117–121.

Garcia Agudo, E., 1998. Global distribution of $^{137}$Cs inputs for soil erosion and sedimentation studies. International Atomic Energy Agency (IAEA).

Geyh, M.A., Schotterer, U., Grosjean, M., 1997. Temporal Changes of the $^{14}$C Reservoir Effect in Lakes. Radiocarbon 40 (2), 921–931.

Glasser, N.F., Jansson, K.N., Goodfellow, B.W., de Angelis, H., Rodnight, H., Rood, D.H., 2011. Cosmogenic nuclide exposure ages for moraines in the Lago San Martin Valley. Argentina. Quat. Res. 75 (3), 636–646.

Goldberg, E.D., 1962. Geochronology with $^{210}$Pb, in: Radioactive Dating. International Atomic Energy Agency Symposium Proceeding, Vienna.

Goldberg, E.D., Gamble, E., Griffin, J.J., Koide, M., 1977. Pollution history of Narragansett Bay as recorded in its sediments. Estuar. Coast. Mar. Sci. 5 (4), 549–561.

Gosse, J.C., Phillips, F.M., 2001. Terrestrial in situ cosmogenic nuclides:theory and application. Quat. Sci. Rev. 20 (14), 1475–1560.

Goswami, V., Hannah, J.L., Stein, H.J., 2018. Why terrestrial coals cannot be dated using the Re-Os geochronometer: Evidence from the Finnmark Platform, southern Barents Sea and the Fire Clay coal horizon, Central Appalachian Basin. Int. J. Coal Geol. 188, 121–135. https://doi.org/10.1016/j.coal.2018.02.005.

Granger, D.E., Kirchner, J.W., Finkel, R., 1996. Spatially Averaged Long-Term Erosion Rates Measured from in Situ-Produced Cosmogenic Nuclides in Alluvial Sediment. J. Geol. 104 (3), 249–257.

Granger, D.E., Smith, A.L., 2000. Dating buried sediments using radioactive decay and muogenic production of 26Al and 10Be. Nucl. Instruments Methods Phys. Res. Sect. B Beam Interact. with Mater. Atoms 172, 822–826. https://doi.org/10.1016/S0168-583X(00)00087-2.

Graven, H.D., Guilderson, T.P., Keeling, R.F., 2012. Observations of radiocarbon in $CO_2$ at seven global sampling sites in the Scripps flask network: Analysis of spatial gradients and seasonal cycles. J. Geophys. Res. Atmos. 117 (D2), n/a–n/a. https://doi.org/10.1029/2011JD016535.

Guilderson, T.P., Cole, J.E., Southon, J.R., 2005. Pre-Bomb $\Delta^{14}$C Variability and the Suess Effect in Cariaco Basin Surface Waters as Recorded in Hermatypic Corals. Radiocarbon 47 (1), 57–65.

Hajdas, I., Ivy-Ochs, S., Pickering, R., Preusser, F., 2008. Recent developments in quaternary dating methods. Geogr. Helv. 63, 176–180. https://doi.org/10.5194/gh-63-176-2008.

Hannah, J.L., Bekker, A., Stein, H.J., Markey, R.J., Holland, H.D., 2004. Primitive Os and 2316 Ma age for marine shale: implications for Paleoproterozoic glacial events and the rise of atmospheric oxygen. Earth Planet. Sci. Lett. 225, 43–52. https://doi.org/10.1016/j.epsl.2004.06.013.

Haridas, N.V., Banerji, U.S., K, M., Padmalal, D., 2022. Paleoclimatic and paleoceanographic records from the Bay of Bengal sediments during the last 30 ka. J. Asian Earth Sci. 229, 105169. https://doi.org/10.1016/j.jseaes.2022.105169.

Heaton, T.J., Blaauw, M., Blackwell, P.G., Bronk Ramsey, C., Reimer, P.J., Scott, E.M., 2020a. The IntCal20 Approach to Radiocarbon Calibration Curve Construction: A New Methodology Using Bayesian Splines and Errors-in-Variables. Radiocarbon 62 (4), 821–863. https://doi.org/10.1017/RDC.2020.46.

Heaton, T.J., Köhler, P., Butzin, M., Bard, E., Reimer, R.W., Austin, W.E.N.N., Ramsey, C. B., Grootes, P.M., Hughen, K.A., Kromer, B., Bronk Ramsey, C., Grootes, P.M., Hughen, K.A., Kromer, B., Reimer, P.J., Adkins, J., Burke, A., Cook, M.S., Olsen, J., Skinner, L.C., 2020b. Marine20—the marine radiocarbon age calibration curve (0–55,000 cal BP). Radiocarbon 62, 779–820. https://doi.org/10.1017/RDC.2020.68.

Heisinger, B.P., 1998. Myonen-induzierte produktion von radionukliden. Technischen Universität München.

Hellborg, R., Faarinen, M., Kiisk, M., Magnusson, C.E., Persson, P., Skog, G., Stenström, K., 2003. Accelerator mass spectrometry-An overview. Vacuum 70 (2–3), 365–372. https://doi.org/10.1016/S0042-207X(02)00671-1.

Hellborg, R., Skog, G., 2008. Accelerator mass spectrometry. Mass Spectrom. Rev. 27, 398–427. https://doi.org/10.1002/mas.20172.

Hicks, H.G., Barr, D.W., 1984. Nevada test site fallout atom ratios: $^{240}$Pu/$^{239}$Pu and $^{241}$Pu/$^{239}$Pu. Lawrence Livermore National Lab.

Hippe, K., 2017. Constraining processes of landscape change with combined in situ cosmogenic 14C–10Be analysis. Quat. Sci. Rev. 173, 1–19. https://doi.org/10.1016/j.quascirev.2017.07.020.

Hippe, K., Kober, F., Zeilinger, G., Ivy-Ochs, S., Maden, C., Wacker, L., Kubik, P.W., Wieler, R., 2012. Quantifying denudation rates and sediment storage on the eastern Altiplano, Bolivia, using cosmogenic $^{10}$Be, $^{26}$Al, and in situ $^{14}$C. Geomorphology 179, 58–70. https://doi.org/10.1016/j.geomorph.2012.07.031.

Hodge, E., McDonald, J., Treble, P.C., Levchenko, V.A., Drysdale, R.N., Waring, C., Hua, Q., Fischer, M.J., 2007. Radiocarbon bomb pulse chronologies for young speleothems and implications for rainfall records in southeast Australia. Quat. Int. 167, 170.

Hoffmann, D.L., Beck, J.W., Richards, D.A., Smart, P.L., Singarayer, J.S., Ketchmark, T., Hawkesworth, C.J., 2010. Towards radiocarbon calibration beyond 28 ka using speleothems from the Bahamas. Earth Planet. Sci. Lett. 289 (1-2), 1–10. https://doi.org/10.1016/j.epsl.2009.10.004.

Hogg, A.G., Hua, Q., Blackwell, P.G., Niu, M.u., Buck, C.E., Guilderson, T.P., Heaton, T. J., Palmer, J.G., Reimer, P.J., Reimer, R.W., Turney, C.S.M., Zimmerman, S.R.H., 2013. SHCal13 Southern Hemisphere Calibration, 0–50,000 Years cal BP. Radiocarbon 55 (4), 1889–1903. https://doi.org/10.2458/azu_js_rc.55.16783.

Hong, W., Park, J.H., Sung, K.S., Woo, H.J., Kim, J.K., Choi, H.W., Kim, G.D., 2010. A New 1MV AMS Facility at Kigam. Radiocarbon 52 (2), 243–251. https://doi.org/10.1017/S0033822200045276.

Hou, X., 2018. Liquid scintillation counting for determination of radionuclides in environmental and nuclear application. J. Radioanalytical Nuclear Chemistry.

Springer International Publishing. 318 (3), 1597–1628. https://doi.org/10.1007/s10967-018-6258-6.
Hua, Q., 2009. Radiocarbon: A chronological tool for the recent past. Quat. Geochronol. 4 (5), 378–390. https://doi.org/10.1016/j.quageo.2009.03.006.
Hua, Q., Barbetti, M., 2007. Influence of atmospheric circulation on regional $^{14}CO_2$ differences. J. Geophys. Res. Atmos. 112 (D19) https://doi.org/10.1029/2006JD007898.
Hua, Q., Barbetti, M., Levchenko, V.A., D'Arrigo, R.D., Buckley, B.M., Smith, A.M., 2012. Monsoonal influence on Southern Hemisphere $^{14}CO_2$. Geophys. Res. Lett. 39, L19806. https://doi.org/10.1029/2012GL052971.
Hua, Q., Barbetti, M., Rakowski, A.Z., 2013. Atmospheric Radiocarbon for the Period 1950–2010. Radiocarbon 55 (4), 2059–2072. https://doi.org/10.2458/azu_js_rc.v55i2.16177.
Hughen, K.A., Baillie, M.G.L., Bard, E., Warren Beck, J., Bertrand, C.J.H., Blackwell, P.G., Buck, C.E., Burr, G.S., Cutler, K.B., Damon, P.E., Edwards, R.L., Fairbanks, R.G., Friedrich, M., Guilderson, T.P., Kromer, B., McCormac, G., Manning, S., Bronk Ramsey, C., Reimer, P.J., Reimer, R.W., Remmele, S., Southon, J.R., Stuiver, M., Talamo, S., Taylor, F.W., VAN der Plicht, J., Weyhenmeyer, C.E., 2004. Marine04 marine radiocarbon age calibration, 0–26 cal kyr BP. Radiocarbon 46 (3), 1059–1086.
Hughen, K.A., Overpeck, J.T., Lehman, S.J., Kashgarian, M., Southon, J.R., Peterson, L.C., 1997. A new $^{14}C$ calibration data set for the last deglaciation based on marine VARVES. Radiocarbon 40 (1), 483–494.
Hughey, B.J., Skipper, P.L., Klinkowstein, R.E., Shefer, R.E., Wishnok, J.S., Tannenbaum, S.R., 2000. Low-energy biomedical GC–AMS system for $^{14}C$ and $^{3}H$ detection. Nucl. Instruments Methods Phys. Res. Sect. B Beam Interact. with Mater. Atoms 172 (1–4), 40–46.
Ivanoff, M.D., Toldo, E.E., Figueira, R.C.L., de Lima Ferreira, P.A., 2020. Use of $^{210}Pb$ and $^{137}Cs$ in the assessment of recent sedimentation in Patos Lagoon, southern Brazil. Geo-Marine Lett. https:// 40 (6), 1057–1067.
Ivanovich, M., Harmon, R.S., 1992. Uranium-series disequilibrium: applications to earth, marine, and environmental sciences. 2.
Ivy-Ochs, S., Briner, J.P., 2014. Dating disappearing ice with cosmogenic nuclides. Elements 10 (5), 351–356. https://doi.org/10.2113/gselements.10.5.351.
Ivy-Ochs, S., Kober, F., 2008. Surface exposure dating with cosmogenic nuclides. E&G Quat. Sci. J. 57, 179–209. https://doi.org/10.3285/eg.57.1-2.7.
Izrael, Y.A., Kvasnikova, E.V., Nazarov, I.M., Fridman, S.D., 1994. Global and regional pollution of the former European USSR with cesium-137. Meteorol. i Gidrol. 5–9.
Jain, M., 2009. Extending the dose range: probing deep traps in quartz with 3.06 eV photons. Radiat. Meas. 44 (5-6), 445–452.
Jena, P.S., Bhushan, R., Ajay, S., Bharti, N., Sudheer, A.K., 2022. $^{10}Be$ depositional flux variation in the central Indian Ocean during the last 43 ka. Sci. Total Environ. 802, 149808 https://doi.org/10.1016/j.scitotenv.2021.149808.
Jena, P.S., Bhushan, R., Shivam, A., Nambiar, R., Bharti, N., 2021. Production rate variation and changes in sedimentation rate of marine core dated with meteoric $^{10}Be$ and $^{14}C$. J. Environ. Radioact. 237, 106678. https://doi.org/10.1016/j.jenvrad.2021.106678.
Jia, G., Belli, M., Liu, S., Sansone, U., Xu, C., Rosamilia, S., Xiao, X., Gaudino, S., Chen, L., Yang, H., 2006. The fractionation and determination procedures for the speciation of $^{210}Pb$ and $^{210}Po$ in soil samples. Anal. Chim. Acta 562 (1), 51–58. https://doi.org/10.1016/j.aca.2006.01.058.
Jia, G., Torri, G., 2007. Determination of $^{210}Pb$ and $^{210}Po$ in soil or rock samples containing refractory matrices. Appl. Radiat. Isot. 65 (1), 1–8. https://doi.org/10.1016/j.apradiso.2006.05.007.
Johnsen, S., Clausen, H.B., Dansgaard, W., Gundestrup, N.S., Hammer, C.U., Andersen, U., Andersen, K.K., Hvidberg, C.S., Steffensen, P., White, J., Jouzel, J., Fisher, D., 1997. The $\delta^{18}O$ record along the Greenland Ice Core Project deep ice core and the problem of possible Eemian climatic instability. J. Geophys. Res. 102, 26397–26410.
Joshi, K.B., Banerji, U.S., Dubey, C.P., Oliveira, E.P., 2021a. Heavy minerals in provenance studies: an overview. Arab. J. Geosci. 14, 1–16.
Joshi, K.B., Bhattacharjee, J., Rai, G., Halla, J., Ahmad, T., Kurhila, M., Heilimo, E., Choudhary, A.K., 2017. The diversification of granitoids and plate tectonic implications at the archaean-Proterozoic boundary in the bundelkhand craton, central India. In: Halla, J., Whitehouse, M.J., Ahmad, T., Bagai, Z. (Eds.), Crust-Mantle Interactions and Granitoid Diversification: Insights from Archaean Cratons. Lyell Publication, Geological Society Publication, pp. 123–157.
Joshi, K.B., Goswami, V., Banerji, U.S., Shankar, R., 2021b. Recent Developments in Instrumentation and its application in absolute geochronology : Historical perspective and Overview. J. Asian Earth Sci. 211, 104690 https://doi.org/10.1016/j.jseaes.2021.104690.
Joshi, L.U., Rangarajan, C., Gopalakrishnan, S.S., 1969. Measurement of lead-210 in surface air and precipitation. Tellus 21 (1), 107–112.
Jouzel, J., Masson-Delmotte, V., Cattani, O., Dreyfus, G., Falourd, S., Hoffmann, G., Minster, B., Nouet, J., Barnola, J.M., Chappellaz, J., Fischer, H., Gallet, J.C., Johnsen, S., Leuenberger, M., Loulergue, L., Luethi, D., Oerter, H., Parrenin, F., Raisbeck, G., Raynaud, D., Schilt, A., Schwander, J., Selmo, E., Souchez, R., Spahni, R., Stauffer, B., Steffensen, J.P., Stenni, B., Stocker, T.F., Tison, J.L., Werner, M., Wolff, E.W., 2007. Orbital and millennial Antarctic climate variability over the past 800,000 years. Science 317 (5839), 793–796. https://doi.org/10.1126/science.1141038.
Jull, A., Burr, G., 2015. Accelerator mass spectrometry. Encycl. Earth Sci. Ser. 3–6.
Jull, A.J.T., 2014. Radiometric Dating Techniques, Reference Module in Earth Systems and Environmental Sciences. Elsevier Inc. Reference Module in Earth Systems and Environmental Sciences. Elsevier.
Jull, A.J.T., Burr, G.S., 2006. Accelerator mass spectrometry: Is the future bigger or smaller? Earth Planet. Sci. Lett. 243 (3-4), 305–325. https://doi.org/10.1016/j.epsl.2005.12.018.
Jull, A.J.T., Wilson, A.E., Burr, G.S., Toolin, L.J., Donahue, D.J., 1992. Measurements of Cosmogenic $^{14}C$ Produced by Spallation in High-Altitude Rocks. Radiocarbon 34 (3), 737–744.
Kaeriyama, H., Shimizu, Y., Ambe, D., Masujima, M., Shigenobu, Y., Fujimoto, K., Ono, T., Nishiuchi, K., Taneda, T., Kurogi, H., Setou, T., Sugisaki, H., Ichikawa, T., Hidaka, K., Hiroe, Y., Kusaka, A., Kodama, T., Kuriyama, M., Morita, H., Nakata, K., Morinaga, K., Morita, T., Watanabe, T., 2014. Southwest intrusion of $^{134}Cs$ and $^{137}Cs$ derived from the Fukushima Dai-ichi nuclear power plant accident in the western North Pacific. Environ. Sci. Technol. 48 (6), 3120–3127. https://doi.org/10.1021/es403686v.
Kawamura, H., Kobayashi, T., Furuno, A., In, T., Ishikawa, Y., Nakayama, T., Shima, S., Awaji, T., 2011. Preliminary numerical experiments on oceanic dispersion of $^{131}I$ and $^{137}Cs$ discharged into the ocean because of the fukushima daiichi nuclear power plant disaster. J. Nucl. Sci. Technol. 48 (11), 1349–1356. https://doi.org/10.1080/18811248.2011.9711826.
Kent, A., 1962. Letters to the editor. Am. Doc. 13 (4), 453. https://doi.org/10.1002/asi.5090130418.
Khandaker, M., Khandaker, M.U., 2011. High purity germanium detector in gamma-ray spectrometry. Ijfps 1, 42–46. https://doi.org/10.14331/ijfps.2012.330011.
Kirchener, G., Ehlers, H., 1998. Sediment Geochronology in Changing Coastal Environments: Potentials and Limitations of the $^{137}CS$ and $^{210}Pb$ Methods. J. Coast. Res. 14, 483–492.
Kirchner, G., 2011. Pb as a tool for establishing sediment chronologies : examples of potentials and limitations of conventional dating models. J. Environ. Radioact. 102, 490–494. https://doi.org/10.1016/j.jenvrad.2010.11.010.
Klein, J., Lerman, J.C., Damon, P.E., Ralph, E.K., 1982. Calibration of radiocarbon dates. Radiocarbon 24, 103–150.
Klein, M.G., Gottdang, A., Mous, D.J.W., Bourlès, D.L., Arnold, M., Hamelin, B., Aumaître, G., Braucher, R., Merchel, S., Chauvet, F., 2008. Performance of the HVE 5 MV AMS system at CEREGE using an absorber foil for isobar suppression. Nucl. Instruments Methods Phys. Res. Sect. B Beam Interact. with Mater. Atoms 266 (8), 1828–1832. https://doi.org/10.1016/j.nimb.2007.11.077.
Knoll, G.F., 1999. Radiation detection and measurement, 3rd ed. Jonh Wiley & Sons, New York.
Kober, F., Ivy-Ochs, S., Schlunegger, F., Baur, H., Kubik, P.W., Wieler, R., 2007. Denudation rates and a topography-driven rainfall threshold in northern Chile: Multiple cosmogenic nuclide data and sediment yield budgets. Geomorphology 83, 97–120. https://doi.org/10.1016/j.geomorph.2006.06.029.
Köhler, M., Preuße, W., Gleisberg, B., Schäfer, I., Heinrich, T., Knobus, B., 2002. Comparison of methods for the analysis of 226Ra in water samples. Appl. Radiat. Isot. 56 (1-2), 387–392.
Kohler, P., Muscheler, R., Fischer, H., 2006. A model-based interpretation of low-frequency changes in the carbon cycle during the last 120,000 years and its implications for the reconstruction of atmospheric $\Delta^{14}C$. Geochemistry Geophys. Geosystems 7, Q11N06. https://doi.org/10.1029/2005GC001228.
Koide, M., Bruland, K.W., Goldberg, E.D., 1973. Th-228/Th-232 and Pb-210 geochronologies in marine and lake sediments. Geochim. Cosmochim. Acta 37 (5), 1171–1187. https://doi.org/10.1016/0016-7037(73)90054-9.
Koide, M., Soutar, A., Goldberg, E.D., 1972. Marine geochronology with $^{210}Pb$. Earth Planet. Sci. Lett. 14 (3), 442–446. https://doi.org/10.1016/0012-821X(72)90146-X.
Koizumi, A., Harada, K.H., Niisoe, T., Adachi, A., Fujii, Y., Hitomi, T., Kobayashi, H., Wada, Y., Watanabe, T., Ishikawa, H., 2012. Preliminary assessment of ecological exposure of adult residents in Fukushima Prefecture to radioactive cesium through ingestion and inhalation. Environ. Health Prev. Med. 17 (4), 292–298. https://doi.org/10.1007/s12199-011-0251-9.
Krey, P.W., Hardy, E.P., Pachucki, C., Rourke, F., Coluzza, J., Benson, W.K., 1976. Mass isotopic composition of global fall-out plutonium in soil, in: Transuranium Nuclides in the Environment.
Krishnaswamy, S., Lal, D., Martin, J.M., Meybeck, M., 1971. Geochronology of lake sediments. Earth Planet. Sci. Lett. 11 (1-5), 407–414.
Kubik, P.W., Ivy-Ochs, S., Masarik, J., Frank, M., Schlüchter, C., 1998. $^{10}Be$ and $^{26}Al$ production rates deduced from an instantaneous event within the dendro-calibration curve, the landslide of Köfels, Ötz Valley. Austria. Earth Planet. Sci. Lett. 161, 231–241. https://doi.org/10.1016/S0012-821X(98)00153-8.
Kudo, A., 2001. Plutonium in the Environment. Elsevier.
Kusakabe, M., Oikawa, S., Takata, H., Misonoo, J., 2013. Spatiotemporal distributions of Fukushima-derived radionuclides in nearby marine surface sediments. Biogeosciences 10 (7), 5019–5030. https://doi.org/10.5194/bg-10-5019-201310.5194/bg-10-5019-2013-supplement.
Kutschera, W., 2016. Accelerator mass spectrometry: state of the art and perspectives. Adv. Phys. X 1 (4), 570–595. https://doi.org/10.1080/23746149.2016.1224603.
Kutschera, W., 2013. Applications of accelerator mass spectrometry. Int. J. Mass Spectrom. 349–350, 203–218. https://doi.org/10.1016/j.ijms.2013.05.023.
Lal, D., 1991. Cosmic ray labeling of erosion surfaces: in situ nuclide production rates and erosion models. Earth Planet. Sci. Lett. 104, 424–439. https://doi.org/10.1016/0012-821X(91)90220-C.
Lal, D., Peters, B., 1967. Cosmic ray produced radioactivity on the Earth. Kosmische Strahlung II/Cosmic Rays II. Springer 551–612.
Lal, D., Peters, B., 1962. Cosmic ray produced isotopes and their application to problems in geophysics. Progr. Elem. Part. Cosm, Ray Phys, p. 6.
Lehto, J., Hou, X., 2011a. Radionuclides and their radiometric measurement. Chem. Anal. radionuclides 1–24.

Lehto, J., Hou, X., 2011b. Chemistry and analysis of radionuclides: laboratory techniques and methodology. John Wiley & Sons.
Levin, I., Hesshaimer, V., 2000. Radiocarbon - A unique tracer of global carbon cycle dynamics. Radiocarbon 42 (1), 69–80. https://doi.org/10.1017/S0033822200053066.
Levin, I., Naegler, T., Kromer, B., Diehl, M., Francey, R., Gomez-Pelaez, A., Steele, P., Wagenbach, D., Weller, R., Worthy, D., 2010. Observations and modelling of the global distribution and long-term trend of atmospheric $^{14}CO_2$. Tellus B: Chemical and Physical Meteorology 62 (1), 26–46. https://doi.org/10.1111/j.1600-0889.2009.00446.x.
Libby, W.F., 1955. Radiocarbon dating, II. ed. University of Chicago Press.
Libby, W.F., 1952. Chicago radiocarbon dates, III. Science 116 (3025), 673–681.
Lifton, N.A., Jull, A.J.T., Quade, J., 2001. A new extraction technique and production rate estimate for in situ cosmogenic $^{14}C$ in quartz. Geochim. Cosmochim. Acta 65, 1953–1969. https://doi.org/10.1016/S0016-7037(01)00566-X.
Lima, A.L., Hubeny, J.B., Reddy, C.M., King, J.W., Hughen, K.A., Eglinton, T.I., 2005. High-resolution historical records from Pettaquamscutt River basin sediments: 1. $^{210}Pb$ and varve chronologies validate record of $^{137}Cs$ released by the Chernobyl accident. Geochim. Cosmochim. Acta 69 (7), 1803–1812. https://doi.org/10.1016/j.gca.2004.10.009.
Lisiecki, L.E., Raymo, M.E., 2005. A Pliocene-Pleistocene stack of 57 globally distributed benthic $\delta^{18}O$ records. Paleoceanography 20 (1), PA1003. https://doi.org/10.1029/2004PA001071.
Livingston, H.D., Povinec, P.P., 2000. Anthropogenic marine radioactivity. Ocean. Coast. Manag. 43 (8-9), 689–712. https://doi.org/10.1016/S0964-5691(00)00054-5.
Longmore, M.E., 1982. The caesium-137 dating technique and associated applications in Australia-a review. Archaeometry. An Australasian Perspective.
Loutre, M.-F., 2009. Precession, Climatic, in: Gornitz, V. (Ed.), Encyclopedia of Paleoclimatology and Ancient Environments. Springer Netherlands, Dordrecht, pp. 825–826. https://doi.org/10.1007/978-1-4020-4411-3_194.
Ma, L., Abuduwaili, J., Liu, W., 2020. Environmentally sensitive grain-size component records and its response to climatic and anthropogenic influences in Bosten Lake region. Sci Rep 10 (1). https://doi.org/10.1038/s41598-020-57921-y.
Mabit, L., Benmansour, M., Abril, J.M., Walling, D.E., Meusburger, K., Iurian, A.R., Bernard, C., Tarján, S., Owens, P.N., Blake, W.H., Alewell, C., 2014. Fallout $^{210}Pb$ as a soil and sediment tracer in catchment sediment budget investigations: A review. Earth-Science Rev. 138, 335–351. https://doi.org/10.1016/j.earscirev.2014.06.007.
Mabit, L., Benmansour, M., Walling, D.E., 2008. Comparative advantages and limitations of the fallout radionuclides $^{137}Cs$, $^{210}Pb_{ex}$ and $^{7}Be$ for assessing soil erosion and sedimentation. J. Environ. Radioact. 99, 1799–1807. https://doi.org/10.1016/j.jenvrad.2008.08.009.
Pheiffer Madsen, P., Sørensen, J., 1979. Validation of the lead-210 dating method. J. Radioanal. Chem. 54 (1-2), 39–48. https://doi.org/10.1007/BF02517759.
Mazeika, J., Duđauskienë-Duz, R., Radzevicius, R., 2004. Sedimentation in the eastern Baltic sea: Lead-210 dating and trace element data implication. Baltica 17, 79–92.
Meijer, H.A.J., Van Der Plicht, J., Gislefoss, J.S., Nydal, R., 1995. Comparing long-term atmospheric 14C and 3H records near Groningen, the Netherlands with Fruholmen, Norway and Izana, Canary Islands 14C stations. Radiocarbon. https://doi.org/10.1017/S0033822200014776.
Mikalauskiene, R., Mažeika, J., Petrošius, R., Szwarczewski, P., 2018. Comparison of beta (LSC) and gamma (HPGe) spectrometric methods for lead-210 in chronological study. Geochronometria 45, 38–50. https://doi.org/10.1515/geochr-2015-0084.
Miller, G.H., Briner, J.P., Lifton, N.A., Finkel, R.C., 2006. Limited ice-sheet erosion and complex in situ cosmogenic Be-10, Al-26, and C-14 on Baffin Island, Arctic Canada. Quat. Geochronol. 1, 74–85.
Morino, Y., Ohara, T., Nishizawa, M., 2011. Atmospheric behavior, deposition, and budget of radioactive materials from the Fukushima Daiichi nuclear power plant in March 2011. Geophysical research letters 38.
Morris, J.D., 1991. Applications of cosmogenic $^{10}Be$ to problems in the earth sciences. Annu. Rev. Earth Planet. Sci. 19 (1), 313–350.
Mudd, S.M., 2017. Detection of transience in eroding landscapes. Earth Surf. Process. Landforms 42 (1), 24–41. https://doi.org/10.1002/esp.3923.
Muller, R.A., Stephenson, E.J., Mast, T.S., 1978. Radioisotope dating with an accelerator: a blind measurement. Science 201 (4353), 347–348.
Muzikar, P., 2020. Exposure-age and erosion rate determination using the in-situ nuclide pair $^{10}Be$–$^{14}C$. Quat. Geochronol. 58, 101076. https://doi.org/10.1016/j.quageo.2020.101076.
Nicolotti, A, 2019. The Shroud of Turin-The history and legends of the world's most famous relic. Baylor University Press, Waco, Texas 76798.
Nishiizumi, K., Winterer, E.L., Kohl, C.P., Klein, J., Middleton, R., Lal, D., Arnold, J.R., 1989. Cosmic ray production rates of $^{10}Be$ and $^{26}Al$ in quartz from glacially polished rocks. J. Geophys. Res. Solid Earth 94, 17907–17915. https://doi.org/10.1029/JB094iB12p17907.
Nydal, Reidar, 1963. Increase in radiocarbon from the most recent series of thermonuclear tests. Nature 200 (4903), 212–214. https://doi.org/10.1038/200212a0.
Owen, L.A., Caffee, M.W., Bovard, K.R., Finkel, R.C., Sharma, M.C., 2006. Terrestrial cosmogenic nuclide surface exposure dating of the oldest glacial successions in the Himalayan orogen: Ladakh Range, northern India. Geol. Soc. Am. Bull. 118 (3-4), 383–392.
Pazdur, A., Nakamura, T., Pawełczyk, S., Pawlyta, J., Piotrowska, N., Rakowski, A., Sensuła, B., Szczepanek, M., 2007. Carbon isotopes in tree rings: Climate and the suess effect interferences in the last 400 years. Radiocarbon 49 (2), 775–788. https://doi.org/10.1017/S003382220004265X.
Perkins, R.W., Thomas, C.W., 1980. Worldwide fallout. Transuranic Elem, Environ.
Petit, J.R., Jouzel, J., Raynaud, D., Barkov, N.I., Barnola, J.M., Basile, I., Bender, M., Chappellaz, J., Davis, M., Delaygue, G., Delmotte, M., Kotlyakov, V.M., Legrand, M., Lipenkov, V.Y., Lorius, C., PÉpin, L., Ritz, C., Saltzman, E., Stievenard, M., 1999. Climate and atmospheric history of the past 420,000 years from the Vostok ice core. Nature 399 (6735), 429–436. https://doi.org/10.1038/20859.
Phillips, F.M., Zreda, M.G., Smith, S.S., Elmore, D., Kubik, P.W., Sharma, P., 1990. Cosmogenic chlorine-36 chronology for glacial deposits at Bloody Canyon, eastern Sierra Nevada. Science (80-. 248 (4962), 1529–1532.
Preiss, N., Mélières, M.A., Pourchet, M., 1996. A compilation of data on lead 210 concentration in surface air and fluxes at the air-surface and water-sediment interfaces. J. Geophys. Res. Atmos. 101 (D22), 28847–28862.
Purser, K.H., Liebert, R.B., Litherland, A.E., Beukens, R.P., Gove, H.E., Bennett, C.L., Clover, M.R., Sondheim, W.E., 1977. An attempt to detect stable N-ions from a sputter ion source and some implications of the results for the design of tandems for ultra-sensitive carbon analysis. Rev. Phys. Appl. 12 (10), 1487–1492.
Purser, K.H., Liebert, R.B., Russo, C.J., 1980. MACS: An accelerator-based radioisotope measuring system. Radiocarbon 22 (3), 794–806.
Purser, K.H., Schneider, R.J., Dobbs, J.M., Post, R., 1981. A preliminary description of a dedicated commercial ultra-sensitive HASS spectrometer, in: The Area of Accelerator Aass Spectroawtry Has Expanded Considerably over the Past Few Years and, Iˆ Our Opinion, Indeed Established Itself as an Independent and Interdisciplinary Research Field. Three Years Have Passed since the First Meeting Was Held At . p. 431.
Purser, K.H., Smick, T.H., Purser, R.K., 1990. A precision $^{14}C$ accelerator mass spectrometer. Nucl. Instruments Methods Phys. Res. Sect. B Beam Interact. Mater. Atoms 52 (3–4), 263–268.
Rahaman, W., Wittmann, H., von Blanckenburg, F., 2017. Denudation rates and the degree of chemical weathering in the Ganga River basin from ratios of meteoric cosmogenic $^{10}Be$ to stable $^{9}Be$. Earth Planet. Sci. Lett. 469, 156–169. https://doi.org/10.1016/j.epsl.2017.04.001.
Raisbeck, G.M., Yiou, F., Fruneau, M., Loiseaux, J.M., Lieuvin, M., Ravel, J.C., 1981. Cosmogenic $^{10}Be/^{7}Be$ as a probe of atmospheric transport processes. Geophys. Res. Lett. 8 (9), 1015–1018.
Raisbeck, G.M., Yiou, F., Fruneau, M., Loiseaux, J.M., Lieuvin, M., Ravel, J.C., Reyss, J. M., Guichard, F., 1980. $^{10}Be$ concentration and residence time in the deep ocean. Earth Planet. Sci. Lett. 51 (2), 275–278.
Bronk Ramsey, C., 2009. Bayesian analysis of radiocarbon dates. Radiocarbon 51 (1), 337–360.
Bronk Ramsey, C., Staff, R.A., Bryant, C.L., Brock, F., Kitagawa, H., van der Plicht, J., Schlolaut, G., Marshall, M.H., Brauer, A., Lamb, H.F., Payne, R.L., Tarasov, P.E., Haraguchi, T., Gotanda, K., Yonenobu, H., Yokoyama, Y., Tada, R., Nakagawa, T., 2012. A complete terrestrial radiocarbon record for 11.2 to 52.8 kyr B.P. Science 338 (6105), 370–374.
Reimer, P.J., 2021. Evolution of Radiocarbon Calibration. Radiocarbon 00. https://doi.org/10.1017/RDC.2021.62.
Raj, H., Bhushan, R., Banerji, U.S., Muruganantham, M., Shah, C., Nambiar, R., Dabhi, A. J., 2022a. Air-sea $CO_2$ exchange rate in the northern Indian Ocean based on coral radiocarbon records. Appl. Geochemistry 137, 105208. https://doi.org/10.1016/j.apgeochem.2022.105208.
Raj, H., Bhushan, R., Kumar, S., Banerji, U.S., Shah, C., Verma, S., 2022b. Monsoon signature in corals from the northern Indian Ocean. J. Mar. Syst. 226, 103664. https://doi.org/10.1016/j.jmarsys.2021.103664.
Ray, S., Joshi, K.B., Sundarraman, S., Joshi, D., Ahmad, T., 2015. Geochemical and petrogenetic study of Proterozoic Sewariya and Govindgarh granitoids from South Delhi Fold Belt. Curr. Sci. 109 https://doi.org/10.18520/v109/i8/1458-1465.
Reimer, P.J., 2020. Composition and consequences of the IntCal20 radiocarbon calibration curve. Quat. Res. (United States) 96, 22–27. https://doi.org/10.1017/qua.2020.42.
Reimer, P.J., Baillie, M.G.L., Bard, E., Bayliss, A., Beck, J.W., Bertrand, C.J.H., Blackwell, P.G., Buck, C.E., Burr, G.S., Cutler, K.B., Damon, P.E., Edwards, R.L., Fairbanks, R.G., Friedrich, M., Guilderson, T.P., Hogg, A.G., Hughen, K.A., Kromer, B., 2004a. Intcal04 terrestrial radiocarbon age calibration, 0–26 cal kyr BP. Radiocarbon 46, 1029–1058.
Reimer, P.J., Baillie, M.G.L., Bard, E., Bayliss, A., Beck, J.W., Blackwell, P.G., Bronk Ramsey, C., Buck, C.E., Burr, G.S., Edwards, R.L., Friedrich, M., Grootes, P.M., Guilderson, T.P., Hajdas, I., Heaton, T.J., Hogg, A.G., Hughen, K.A., Kaiser, K.F., Kromer, B., McCormac, F.G., Manning, S.W., Reimer, R.W., Richards, D.A., Southon, J.R., Talamo, S., Turney, C.S.M., van der Plicht, J., Weyhenmeyer, C.E., 2009. IntCal09 and Marine09 Radiocarbon Age Calibration Curves, 0–50,000 Years cal BP. Radiocarbon 51 (4), 1111–1150.
Reimer, P.J., Bard, E., Bayliss, A., Beck, J.W., Blackwell, P.G., Bronk Ramsey, C., Buck, C. E., Cheng, H., Edwards, R.L., Friedrich, M., Grootes, P.M., Guilderson, T.P., Haflidason, H., Hajdas, I., Hatté, C., Heaton, T.J., Hoffmann, D.L., Hogg, A.G., Hughen, K.A., Kaiser, K.F., Kromer, B., Manning, S.W., Niu, M., Reimer, R.W., Richards, D.A., Scott, E.M., Southon, J.R., Staff, R.A., Turney, C.S.M., van der Plicht, J., 2013. IntCal13 and Marine13 Radiocarbon Age Calibration Curves 0–50,000 Years cal BP. Radiocarbon 55, 1869–1887. https://doi.org/10.1017/S0033822200048864.
Reimer, P.J., Brown, T.A., Reimer, R.W., 2004b. Discussion: Reporting and calibration of post-bomb $^{14}C$ data. Radiocarbon 46, 1299–1304. https://doi.org/10.1017/S0033822200033154.
Robbins, J.A., 1978. Geochemical and geophysical applications of radioactive lead. In: Biogeochemistry of Lead in the Environment. Elsevier Scientific, pp. 285–393.
Robbins, J.A., Edgington, D.N., 1975. Determination of recent sedimentation rates in Lake Michigan using Pb-210 and Cs-137. Geochemica Cosmochim. Acta 39 (3), 285–304.

Roth, R., Joos, F., 2013. A reconstruction of radiocarbon production and total solar irradiance from the Holocene $^{14}C$ and $CO_2$ records: Implications of data and model uncertainties. Clim. Past. https://doi.org/10.5194/cp-9-1879-2013.

Rypina, I.I., Jayne, S.R., Yoshida, S., Macdonald, A.M., Douglass, E., Buesseler, K., 2013. Short-term dispersal of Fukushima-derived radionuclides off Japan: modeling efforts and model-data intercomparison. Biogeosciences 10 (7), 4973–4990. https://doi.org/10.5194/bg-10-4973-2013.

Saenko, V., Ivanov, V., Tsyb, A., Bogdanova, T., Tronko, M., Demidchik, Y.u., Yamashita, S., 2011. Overview of the Chernobyl accident and its consequences. Clin. Oncol. 23 (4), 234–243.

Samom, J.D., Ahmad, T., Choudhary, A.K., 2018. Geochemical and Sm-Nd isotopic constraints on the petrogenesis and tectonic setting of the Proterozoicmafic magmatism of the Gwalior Basin, central India: The influence of Large Igneous Provinces on Proterozoic crustal evolution. Geol. Soc. Spec. Publ. 463 (1), 243–268. https://doi.org/10.1144/SP463.10.

Saunders, I., Young, A., 1983. Rates of surface processes on slopes, slope retreat and denudation. Earth Surf. Process. Landforms 8 (5), 473–501. https://doi.org/10.1002/esp.3290080508.

Shackleton, N.J., Berger, A., Peltier, W.R., 1990. An alternative astronomical calibration of the lower Pleistocene timescale based on ODP Site 677. Earth Environ. Sci. Trans. R. Soc. Edinburgh 81 (4), 251–261.

Shah, C., Banerji, U.S., Chandana, K.R., Bhushan, R., 2020. $^{210}Pb$ dating of recent sediments from the continental shelf of western India : factors influencing sedimentation rates. Environ. Monit. Assess. 192, 468.

Shaji, J., Banerji, U.S., Maya, K., Joshi, K.B., Dabhi, A.J., Bharti, N., Bhushan, R., Padmalal, D., 2022. Holocene monsoon and sea-level variability from coastal lowlands of Kerala, SW India. Quat. Int. https://doi.org/10.1016/j.quaint.2022.03.005.

Simsek, F.B., Cagatay, M.N., 2014. Geochronology of lake sediments using 210 Pb with double energetic window method by LSC : An application to Lake Van. Appl. Radiat. Isot. 93, 126–133. https://doi.org/10.1016/j.apradiso.2014.01.028.

Singh, K.T., Nayak, G.N., Fernandes, L.L., Borole, D.V., Basavaiah, N., 2014. Changing environmental conditions in recent past-Reading through the study of geochemical characteristics, magnetic parameters and sedimentation rate of mudflats, central west coast of India. Palaeogeogr. Palaeoclimatol. Palaeoecol. 397, 61–74. https://doi.org/10.1016/j.palaeo.2013.04.008.

Small, E.E., Anderson, R.S., Repka, J.L., Finkel, R., 1997. Erosion rates of alpine bedrock summit surfaces deduced from in situ $^{10}Be$ and $^{26}Al$. Earth Planet. Sci. Lett. 150, 413–425. https://doi.org/10.1016/S0012-821X(97)00092-7.

Smith, J.N., Walton, A., 1980. Sediment accumulation rates and geochronologies measured in the Saguenay Fjord using the Pb-210 dating method. Geochim. Cosmochim. Acta 44 (2), 225–240.

Somayajulu, B.L.K., Bhushan, R., Sarkar, A., Burr, G.S., Jull, A.J.T., 1999. Sediment deposition rates on the continental margins of the eastern Arabian Sea using $^{210}Pb$, $^{137}Cs$ and $^{14}C$. Sci. Total Environ. 237-238, 429–439.

Somayajulu, B.L.K., Yadav, D.N., Sarin, M.M., 1994. Recent sedimentary records from the Arabian Sea. Indian Acad. Sci. - Earth Planet. Sci. 103 (2), 315–327. https://doi.org/10.1007/BF02839541.

Southon, J., Noronha, A.L., Cheng, H., Edwards, R.L., Wang, Y., 2012. A high-resolution record of atmospheric $^{14}C$ based on Hulu Cave speleothem H82. Quat. Sci. Rev. 33, 32–41. https://doi.org/10.1016/j.quascirev.2011.11.022.

Srivastava, T., Joshi, K.B., Wanjari, N, 2022. Boron isotopic composition of pegmatitic tourmaline from Yumthang valley, North Sikkim, India. In: John, A.A., Kailasa, P., Verma, S.K. (Eds.), Geochemical Treasures and Petrogenetic processes. Springer Nature. In press.

Stan-Sion, C., Enachescu, M., Petre, A.R., Simion, C.A., Calinescu, C.I., Ghita, D.G., 2015. A new and compact system at the AMS laboratory in Bucharest. Nucl. Instruments Methods Phys. Res. Sect. B Beam Interact. with Mater. Atoms 361, 105–109. https://doi.org/10.1016/j.nimb.2015.02.059.

Stuiver, M., 1982. A high-precision calibration of the AD radiocarbon time scale. Radiocarbon 24 (1), 1–26.

Stuiver, M., Braziunas, T.F., 1993. Modeling atmospheric $^{14}C$ influences and $^{14}C$ ages of marine samples to 10,000 BC. Radiocarbon 35, 137.

Stuiver, M., Braziunas, T.F., 1989. Atmospheric $^{14}C$ and century-scale solar oscillations. Nature 338 (6214), 405–408. https://doi.org/10.1038/338405a0.

Stuiver, M., Pearson, G.W., Braziunas, T., 1986. Radiocarbon age calibration of marine samples back to 9000 cal yr BP. Radiocarbon 28 (2B), 980–1021.

Stuiver, M., Polach, H.A., 1977. Reporting of $^{14}C$ data. Radiocarbon 19, 355–363.

Stuiver, M., Quay, P.D., 1981. Atmospheric $^{14}C$ changes resulting from fossil fuel $CO_2$ release and cosmic ray flux variability. Earth Planet. Sci. Lett. 53 (3), 349–362. https://doi.org/10.1016/0012-821X(81)90040-6.

Stuiver, M., Reimer, P.J., Bard, E., Beck, J.W., Burr, G.S., Hughen, K.A., Kromer, B., McCormac, G., Van Der Plicht, J., Spurk, M., 1998a. INTCAL98 radiocarbon age calibration, 24,000–0 cal BP. Radiocarbon 40 (3), 1041–1083. https://doi.org/10.1017/S0033822200019123.

Stuiver, M., Reimer, P.J., Braziunas, T.F., 1998b. High-precision radiocarbon age calibration for terrestrial and marine samples. Radiocarbon 40 (3), 1127–1151.

Suess, H.E., 1955. Radiocarbon concentration in modern wood. Science 122 (3166), 415–417.

Richard, A.M., Alvarez, L.W., Holley, W.R., Stephenson, E.J., 1976. Quarks with unit charge: a search for anomalous hydrogen. Sci. Mag. 196, 521–523.

Swarzenski, P.W., Baskaran, M., Rosenbauer, R.J., Orem, W.H., 2006. Historical trace element distribution in sediments from the Mississippi River Delta. Estuaries and Coasts 29 (6), 1094–1107. https://doi.org/10.1007/BF02781812.

Tans, P.P., De jong, A.F.M., Mook, W.G., 1979. Natural atmospheric $^{14}C$ variation and the Suess effect. Nature 280 (5725), 826–828. https://doi.org/10.1038/280826a0.

Thomsen, K.J., Murray, A.S., Jain, M., Bøtter-Jensen, L., 2008. Laboratory fading rates of various luminescence signals from feldspar-rich sediment extracts. Radiat. Meas. 43 (9-10), 1474–1486. https://doi.org/10.1016/j.radmeas.2008.06.002.

Törnqvist, T.E., Rosenheim, B.E., Hu, P., Fernandez, A.B., 2015. Radiocarbon dating and calibration. Handb. Sea-Level Res. 347–360 https://doi.org/10.1002/9781118452547.ch23.

Tripathy, G.R., Hannah, J.L., Stein, H.J., 2018. Refining the Jurassic-Cretaceous boundary: Re-Os geochronology and depositional environment of Upper Jurassic shales from the Norwegian Sea. Palaeogeogr. Palaeoclimatol. Palaeoecol. 503, 13–25. https://doi.org/10.1016/j.palaeo.2018.05.005.

Tsumune, D., Tsubono, T., Aoyama, M., Hirose, K., 2012. Distribution of oceanic $^{137}Cs$ from the Fukushima Dai-ichi Nuclear Power Plant simulated numerically by a regional ocean model. J. Environ. Radioact. 111, 100–108. https://doi.org/10.1016/j.jenvrad.2011.10.007.

Tsumune, D., Tsubono, T., Aoyama, M., Uematsu, M., Misumi, K., Maeda, Y., Yoshida, Y., Hayami, H., 2013. One-year, regional-scale simulation of $^{137}Cs$ radioactivity in the ocean following the Fukushima Daiichi Nuclear Power Plant accident. Biogeosciences Discuss. 10, 6259–6314. https://doi.org/10.5194/bgd-10-6259-2013.

Tuniz, C., Kutschera, W., Fink, D., Herzog, G.F., Bird, J.R., 1998. Accelerator mass spectrometry: ultrasensitive analysis for global science. CRC Press.

Uemura, R., Motoyama, H., Masson-Delmotte, V., Jouzel, J., Kawamura, K., Goto-Azuma, K., Fujita, S., Kuramoto, T., Hirabayashi, M., Miyake, T., Ohno, H., Fujita, K., Abe-Ouchi, A., Iizuka, Y., Horikawa, S., Igarashi, M., Suzuki, K., Suzuki, T., Fujii, Y., 2018. Asynchrony between Antarctic temperature and $CO_2$ associated with obliquity over the past 720,000 years. Nat. Commun. 9 (1) https://doi.org/10.1038/s41467-018-03328-3.

United Nations, 1982. Ionizing radiation: Sources and biological effects. UNSCEAR Rep.

United Nations, 1969. United Nations Scientific Committee on the Effects of Atomic Radiation 1969, in: Report to the General Assembly, 24th Session. United Nations New York.

UNSCEAR, 2000. Sources and Effects of Ionizing Radiation, United Nations Scientific Committee on the Effects of Atomic Radiation UNSCEAR 2000 Report to the General Assembly, with Scientific Annexes, UNSCEAR 2000 Report. https://doi.org/10.1097/00004032-199907000-00007.

UNSCEAR, A., 1988. United nations scientific committee on the effects of atomic radiation. Sources, Eff. Risks Ioniz. Radiat.

van den Bergh, G.D., Boer, W., Schaapveld, M.A.S., Duc, D.M., van Weering, T.C.E., 2007. Recent sedimentation and sediment accumulation rates of the Ba Lat prodelta (Red River, Vietnam). J. Asian Earth Sci. 29 (4), 545–557. https://doi.org/10.1016/j.jseaes.2006.03.006.

Vanacker, V., von Blanckenburg, F., Hewawasam, T., Kubik, P.W., 2007. Constraining landscape development of the Sri Lankan escarpment with cosmogenic nuclides in river sediment. Earth Planet. Sci. Lett. 253, 402–414. https://doi.org/10.1016/j.epsl.2006.11.003.

Vermeesch, P., 2014. Isotope Geology Part I : Radiometric Geochronology. Isot, Geoloogy https://doi.org/10.31223/osf.io/sj4ft.

Vesterbacka, P., Ikäheimonen, T.K., 2005. Optimization of $^{210}Pb$ determination via spontaneous deposition of $^{210}Po$ on a silver disk. Anal. Chim. Acta 545 (2), 252–261. https://doi.org/10.1016/j.aca.2005.04.074.

Villa, M., Hurtado, S., Manjón, G., García-Tenorio, R., 2007. Calibration and measurement of 210 Pb using two independent techniques. Radiat. Meas. 42, 1552–1560. https://doi.org/10.1016/j.radmeas.2007.05.053.

Villa, M., Hurtado, S., Manjón, G., García-Tenorio, R., García-León, M., 2006. Direct $^{210}Pb$ determination in environmental samples by liquid scintillation counting and its validation through y-ray. In: Chalupnik, S., Schönhofer, F., Noakes, J. (Eds.), Advances in Liquid Scintillation Spectrometry. Arizona Board of Regents on behalf of the University of Arizona, pp. 217–227.

von Blanckenburg, F., 2005. The control mechanisms of erosion and weathering at basin scale from cosmogenic nuclides in river sediment. Earth Planet. Sci. Lett. 237, 462–479. https://doi.org/10.1016/j.epsl.2005.06.030.

Wang, X.L., Wintle, A.G., Lu, Y.C., 2006. Thermally transferred luminescence in fine-grained quartz from Chinese loess: basic observations. Radiat. Meas. 41 (6), 649–658.

Watchman, A.L., Twidale, C.R., 2002. Relative and "absolute" dating of land surfaces. Earth-Science Rev. 58 (1-2), 1–49. https://doi.org/10.1016/S0012-8252(01)00080-0.

White, D., Fülöp, R.-H., Bishop, P., Mackintosh, A., Cook, G., 2011. Can in-situ cosmogenic $^{14}C$ be used to assess the influence of clast recycling on exposure dating of ice retreat in Antarctica? Quat. Geochronol. 6 (3–4), 289–294. https://doi.org/10.1016/j.quageo.2011.03.004.

Williams, M., Dunkerley, D., Deckker, P.D., Kershaw, P., Chappell, J., 1998. Quaternary sea level changes. In: Quaternary Environments. Arbold, London, pp. 107–125.

Wittmann, H., von Blanckenburg, F., 2009. Cosmogenic nuclide budgeting of floodplain sediment transfer. Geomorphology 109 (3-4), 246–256. https://doi.org/10.1016/j.geomorph.2009.03.006.

Xiang, L., Lu, X.X., Higgitt, D.L., Wang, S.M., 2002. Recent lake sedimentation in the middle and lower Yangtze basin inferred from $^{137}Cs$ and $^{210}Pb$ measurements. J. Asian Earth Sci. 21 (1), 77–86. https://doi.org/10.1016/S1367-9120(02)00015-9.

Zaborska, A., Carroll, JoLynn, Papucci, C., Pempkowiak, J., 2007. Intercomparison of alpha and gamma spectrometry techniques used in $^{210}Pb$ geochronology. J. Environ. Radioact. 93 (1), 38–50. https://doi.org/10.1016/j.jenvrad.2006.11.007.

Zimmerman, B.E., Collé, R., Cessna, J.T., 2004. Construction and implementation of the NIST triple-to-double coincidence ratio (TDCR) spectrometer. Appl. Radiat. Isot. 60 (2-4), 433–438.

Zoppi, U., Albani, A., Ammerman, A.J., Hua, Q., Lawson, E.M., Serandrei Barbero, R., 2001. Preliminary Estimate of the Reservoir Age in the Lagoon of Venice. Radiocarbon 43 (2A), 489–494.

Zoppi, U., Skopec, Z., Skopec, J., Jones, G., Fink, D., Hua, Q., Jacobsen, G., Tuniz, C., Williams, A., 2004. Forensic applications of $^{14}$C bomb-pulse dating. Nuclear Instruments and Methods in Physics Research Section B: Beam Interactions with Materials and Atoms 223-224, 770–775.